



Master's Thesis

**Characterization of Neutron Response
of Ionization Chambers**

Manuel Trigueros Galdón





Master's Thesis

**Characterization of Neutron Response
of Ionization Chambers**

**Charakterisierung des Neutronenansprechverhaltens
von Ionisationskammern**

Author: Manuel Trigueros Galdón
Supervisor: Prof. Dr. Peter Müller-Buschbaum
Advisor: Dr. Tobias Chemnitz
Mentor: Dr. Dimitrios Karampinos
Submission Date: December 15th, 2023



Abstract

This thesis studies the sensibility to neutron and gamma radiation of mainly magnesium ionization chambers used in dosimetry for fast neutron therapy. The sensibility happens to be altered, which results in uncertainties in the dosimetric measurements.

The atmospheric conditions cause the development of a corrosion layer on the PTW magnesium chamber TM33054 that leads to a change in the dose delivered by certain particles. This layer might cause an alteration in the sensibility of the magnesium chamber and result in the unsuitability of the device under a β^- check source for daily measurements.

To study the problem, a neutron and a X-ray CT scan were done on the chamber to search for a layer made of another material. A Monte Carlo simulation of the chamber was run after it to investigate how radiation is absorbed per unit mass by its sensitive region in presence of the layer. Additionally, a calibration of the magnesium and tissue equivalent chamber (TE) was performed at Physikalisch-Technische Bundesanstalt (PTB) to calculate their sensibility.

The result of the neutron CT scan confirms the presence of a 0.37 mm thick corrosion layer assumed to consist of hydromagnesite, and the simulations show that the dose absorbed by the magnesium chamber is higher in presence of the layer. A small concentration of water in the layer contributes further to a higher dose deposition. The calibration confirms that the sensibility of the Mg device has increased over the span of 5 years, and challenges the assumption that it remains constant for the TE chambers at 2.5 MeV.

In conclusion, the hydromagnesite layer is the cause of the increased sensibility of the PTW TM33054 magnesium chamber under normal atmospheric conditions. The suitability of the β^- check source remains unchanged for check measurements, regardless of the development of a hydromagnesite layer. The increased sensibility of the tissue equivalent chambers is left as a research object for further work.

I confirm that this master's thesis is my own work and I have documented all sources and material used.

Munich, December 15th, 2023

Manuel Trigueros Galdón

Contents

Abstract	iii
1 Introduction	1
2 Theoretical Foundations	3
2.1 Context about FRM II and MEDAPP	3
2.2 Neutron Interaction with Matter	3
2.2.1 Micro- and Macroscopic Cross Section	4
2.2.2 Interaction Neutron-Nuclei	4
2.2.3 Average Energy Loss	5
2.2.4 Mean Free Path	5
2.3 Neutron Radiation Detection and Ionization Chambers	6
2.3.1 Ionization Chambers	6
2.4 Dosimetric Principles	7
2.4.1 Kerma and Dose	7
2.4.2 Bragg-Gray Cavity Theory	8
2.4.3 Spencer-Attix Cavity Theory	8
2.4.4 The Two Chamber Method	9
2.5 Monte Carlo Simulation	10
2.5.1 MCNP Simulations	11
3 Atmospheric Corrosion of Mg	13
3.1 Corrosion of Ionization Chambers	13
3.2 X-Ray and Neutron Imaging	14
3.3 Simulated Oxidation Layers	16
3.3.1 MEDAPP Source with a Hydromagnesite Corrosion Layer	17
3.3.2 Neutron Source with a Hydromagnesite Corrosion Layer	22
4 Reference Measurements	27
4.1 Calibration Measurements in Neutron Reference Field	27
4.1.1 Data Comparison	30
4.2 Build-up Effect	31
4.2.1 Build-up Effect in Tissue Equivalent Plastic A-150 (TE)	32
4.2.2 Build-up Effect in Magnesium	33
5 Simulated Check Source	37
5.1 ^{90}Sr as a Source	37

5.2	Activity Calculation	39
5.3	Sampling of the Emission Spectrum	40
5.4	Setting up the soure	42
5.5	<i>Bremsstrahlung</i> spectrum	44
5.5.1	Particle Flux	44
5.6	Simulation	47
6	Conclusions and Outlook	49
	Acknowledgments	51
	List of Figures	53
	List of Tables	55
	Bibliography	57

1 Introduction

Over the years there has been a long-standing research of cancer sickness worldwide. Various therapies, both palliative and curative, have been developed to address the disease in different ways. One the principal therapies that has gained the interest of researchers and medical centers is the particle therapy. This therapy is designed and planned by medical physicists in coordination with physicians and consists of irradiating the tissue of interest with a source of particles of different nature, so that the interaction of particle and matter results in a destruction of the malignant cells. Although in radiotherapy treatments several combinations of fundamental particles are susceptible to be used, it is of special interest to look at the case of neutrons only and study their specific interaction with matter. The reason for this decision is the fact that unique therapies that use neutrons for palliative treatments exist in very few places around the globe and succeeded improving the health and life expectancy of the persons who received them.

Treatments performed with neutrons can be divided in two types: Fast Neutron Therapy (FNT) and Boron Neutron Capture Therapy (BNCT). The main stream of patients have gone for FNT worldwide. For five decades, FNT has been applied to more than 30.000 patients and it could be established as a clinical routine therapy that went over the experimental or scientific stage [26]. In the world, one of the few facilities that offer FNT is located at FRM II run by the Technical University of Munich (TUM), located in Garching. The term FRM II stands for Forschungsreaktor München, which means research reactor in German. Regarding the rest of the facilities, by 2015 only three are still present and running: at the UW Medical Center in Seattle (USA), Polytechnic University in Tomsk (Russia) and FRM II in Garching (Germany) [26]. The number of facilities decreased over time due to medical decisions based on the supposed risk of the therapy.

The medical application facility of FRM II (MEDAPP) supplies a beam of fast neutrons created by fission of ^{235}U . The source can be used for medical applications like the irradiation of human cancer, for radiography and CT in non-destructive material characterisation as well as for the irradiation of biological tissue. For such applications, a detailed knowledge of the neutron spectrum is required.

As neutrons cannot directly ionize matter, they need to be converted into charged particles to be detected. The basic physical principles for neutron detection are the neutron's characteristic properties and several important nuclear reactions. This is a common practice that will be used throughout the project.

The neutron detection will be carried out in this project by a gas-filled detector type, which is the ionization chamber. Their normal operation is based on the collection of

the charge created by interaction of radiation in the gas and they are commonly used for medical applications like dosimetry.

The goal of this project is, therefore, to search for corrosion products on the ionization chamber model TM33054 designed by the company PTW, and confirm whether the products affect the reading of the chamber in both clinical applications and daily checks with a β^- source. In order to study the response of the ionization chamber, several steps need to be considered. The first is to run a CT scan on the chambers to search for any corrosion product that might affect the measured dose. The scan images were taken at Munich Institute of Biomedical Engineering with the support of Dr. rer. nat. Klaus Achterhold.

The next step is to perform a Monte Carlo simulation of the chamber to measure the dose absorbed by the gas at sensitive region, which is filled by argon gas. The simulation is made using the Monte Carlo N-Particle code (MCNP), which is a software developed by Los Alamos National Laboratory, and is able to generate a wide variety of geometries and irradiation scenarios. The simulation reproduces the mixed neutron and gamma source used at MEDAPP and the geometry of the chamber.

Lastly, a calibration of the chamber is performed at PTB to measure the sensibility of the PTW TM33054 made of magnesium, and of the PTW TM33053 made of tissue equivalent plastic. This last step is done to check whether the sensibility of the device has increased over time.

2 Theoretical Foundations

2.1 Context about FRM II and MEDAPP

In the past, a total of 715 patients have undergone FNT treatment between 1985 and 2000 at the facilities of FRM, the predecessor of FRM II. The new reactor FRM II became operative in 2005 and the first patient was irradiated at MEDAPP in 2007 [12]. The MEDAPP facility was built to provide similar dosimetric characteristics to the old radiation facility [26].

The treatment consists in irradiating slowly growing and/or well differentiated tumors [27] with fast neutrons at a mean energy of 1.9 MeV. FNT is generally accepted as a palliative treatment of shallow tumor lesions [27] like a carcinoma.

In order to generate the fast neutrons necessary to carry out the treatment, FRM II is equipped with a converter facility that allows their generation. At the reactor, two converter plates containing 540 g highly enriched ^{235}U (93%) [26] are mounted within the D_2O moderator tank in about 1 m distance to the reactor core, which powers the converter with thermal neutrons. In the converter facility, fast neutrons are generated by induced fission of the thermal neutrons with the uranium plates.

The beam that comes out of the converter facility is a mixed radiation field of fast neutrons and gammas. The γ component is undesired for the application of FNT. While several filters exist to reduce the γ -photon contamination, only one can be applied at MEDAPP due to the constraints of the license for medical operations [27].

At MEDAPP, neutrons are almost always administrated combined with conventional photon therapy. In the following subsection, the neutron physics and neutron interaction with matter will be covered in detail.

2.2 Neutron Interaction with Matter

Neutrons expose a large number of properties. Some of those properties, are relevant to the study of their interaction with matter. In the present project, the response of the ionization chambers is described in terms of the cross section, mean free path and energy loss. For this reason, the concepts will be briefly introduced in this section.

2.2.1 Micro- and Macroscopic Cross Section

The cross section is the probability of a scattering or absorption event to occur between a neutron and the nucleus [21]. The probability of each type of event is independent of the others [21]. As a consequence, each probability contributes to the total probability or cross section.

The absorption cross section is the probability of a nucleus of being absorbed, P_{abs} , over the atom density. The mathematical expression is, therefore [21]:

$$\sigma_a = \frac{P_{abs}}{N/A} [\text{cm}^2] \quad (2.1)$$

In Equation 2.1, N and A stand for the total number of target atoms within the area A. The cross section defining the probability of an individual neutron interaction is referred to as *microscopic* cross section. Furthermore, the total (microscopic) cross section is the sum of the absorption and scattering cross section:

$$\sigma_t = \sigma_a + \sigma_s [\text{cm}^2] \quad (2.2)$$

In Equation 2.1, σ_t represents the total probability of any event taking place. σ_a and σ_s , represent the absorption and scattering cross section, respectively. A common unit to measure the cross section is the *barn*. It is represented as b and is equal to 10^{-24} cm^2 . A barn is a unit used simply for the convenience of avoid working with very small numbers, since typical values for the cross section are in the range of 10^{-21} to 10^{-27} cm^2 for heavy nuclei [21].

In this project, only the microscopic cross section, also referred to as simply cross section, is relevant for the understanding of plots and response of the devices.

2.2.2 Interaction Neutron-Nuclei

In nuclear physics, when an interaction occurs, a simple notation is used to provide concise information about the interaction of interest as well as the initial target and products of the nuclear interaction. In the case of study, if a neutron hits a target T and gives as a resultant nucleus and an outgoing particle x , the interaction is shown as [23]:

$$T(n, x) R \quad (2.3)$$

Here, n stands for the incoming neutron, x represents the outgoing particle and T and R , the target and residual nucleus of the heavy nuclei, respectively. The outgoing particle does not necessarily need to be another neutron, or many other particles.

In case of a scattering event, this can be either elastic or inelastic. The de-excitation of a nucleus after inelastic scattering occurs via γ -emission [23]. Following discussions about the energy change of the system take place in the next subsection.

2.2.3 Average Energy Loss

When a neutron whose kinetic energy is E_{kin} encounters a target nucleus of atomic weight A , the average energy loss is equal to [21]:

$$\frac{2 E_{kin} A}{(1 + A)^2} \quad (2.4)$$

In Equation 2.4, it is described the mean energy loss **per collision**. After several collisions with the same target, the neutron will be thermalised i.e. will have its energy reduced.

While a fast neutron needs to collide with a carbon atom an average of over a hundred times to reach thermal equilibrium, it only needs 27 collisions if it does with a hydrogen atom [21]. This means that the average energy loss reaches its maximum in the case of hydrogen. In such case, Equation 2.4 results in:

$$\frac{1}{2} E_{kin} \quad (2.5)$$

According to Equation 2.5, a neutron loses half of its kinetic energy when it collides with a hydrogen atom. For this reason, only the interaction of neutrons and hydrogen is considered in the study of the response of the ionization chambers.

2.2.4 Mean Free Path

In particle physics, the mean free path λ , is the average distance that a moving particle with a cross section σ travels in a medium of density ρ without interacting with any other particle on its way. As it is shown in the next equation, it is inversely proportional to those parameters:

$$\lambda \propto \frac{1}{\sigma \rho} \text{ [m]} \quad (2.6)$$

The mean free path is always relative to the particle and the medium. A shorter mean free path means that the particle will interact multiple times per unit distance, which will affect the dose deposition in the medium.

The reason why "particles" is used over "neutrons" is because the concept of mean free path can be applied to any other particle and it is not a specific property of neutrons.

2.3 Neutron Radiation Detection and Ionization Chambers

In order to investigate the characteristics of particles, it is necessary to rely on particle detectors. Charged particles interact with other particles primarily via Coulomb scattering and are the easiest to detect because of it. Some detectors are designed to measure the ionization produced by charged particles as they pass through a medium [11]. When it comes to neutrons, the detection becomes more complicated. Neutrons do not produce any ionization nor undergo Coulomb scattering. Instead, they interact with the target nucleus via nuclear reactions.

One way to detect neutrons is to cause them to react via nuclear interaction with a material, and then measure the ionization of the medium that the product (charged) particles induce. This is a common design for the so called ionization chambers, the detection device that concerns this work. The neutrons produced from the initial reaction with the target cannot be measured directly for the reason stated previously. Instead, they need to interact again and generate measurable charged particles. Further details will be exposed about ionization chambers in the next subsection.

2.3.1 Ionization Chambers

Ionization chambers are a detector used in dosimetry to measure the dose delivered by a source of radiation [18]. Ionization chambers are a type of gas-filled detector, which is a device that is able to operate at different voltages according to the sensibility of the measurements it is intended to obtain. A gas-filled detector behaves as a ionization chamber at relatively low voltages [11]. Regarding the design, a ionization chambers is a generally cylindrical cavity filled with a gas and contains an electrode placed in the center in the longitudinal direction. The cavity is surrounded by a conductive wall [18]. A commonly used chamber for radiation therapy dosimetry measurements is the 30010 Farmer [3]. The basic design of a Farmer chamber is shown in Figure 2.1.

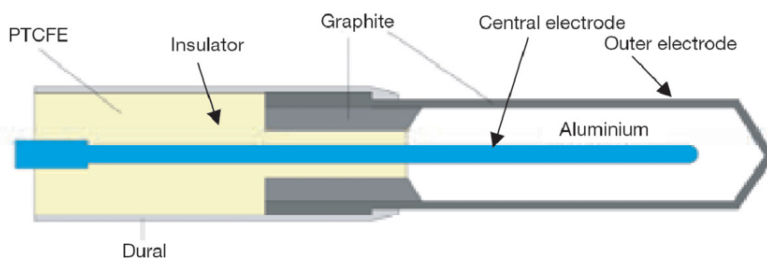


Figure 2.1: Basic design of a Farmer Ionization Chamber.

In Figure 2.1, all the constituent parts of the Farmer are pointed out. The PTCFE is polytrichloro-fluoroethylene [6], an insulator material meant to reduce the leakage current [18]. A graphite sleeve is inserted to eliminate the disturbance caused by the

remaining charges on the insulator [6]. The wall material is generally made of a low Z material to reduce the energy loss. The chamber is covered with a "cap", referred to as "dural" in Figure 2.1 for calibration purposes.

Incoming neutrons generated by a radiation source come into the sensitive region or gas-filled region of chamber and generate charged particles, including electrons and heavy ions. Applying a voltage to the electrode causes the charged particles to be attracted to it and, therefore, an increase in the total charge accumulated in the detector. This is the variable that can be measured to calibrate the device to finally calculate the total dose absorbed by the gas of the chamber.

Ionization chambers are able to provide high resolution measurements in terms of energy because there is no signal amplification. This means that the response of the chamber will be linear, and is due to the voltage that is applied to the electrode. A higher voltage would cause a strong amplification or even an avalanche effect in the charges present in the environment within the sensitive region [11].

2.4 Dosimetric Principles

Having provided an overview of the neutron radiation and its interaction with matter, it is fundamental to go through the aspect of the dose deposition in tissue by neutron radiation and provide some background about the dosimetry methods used at MEDAPP.

It makes sense to introduce in this section the concept of dose and briefly explain why it is relevant in the scope of this work. Dosimetry is, in radiology, the measurement and assessment of the absorbed dose i.e. the amount of energy delivered per gram of matter, of ionizing and nuclear radiation source to a tissue. The importance of the determination of the dose lies totally in the biological direct and side effects that radiation has. Radiation is able to interrupt the biological cycle of cancerous cells and, therefore serve as an effective treatment to cancer disease. It is, hence, of crucial importance to determine the dose delivered by a source with as much precision as possible.

2.4.1 Kerma and Dose

In the context of medical physics, kerma is the acronym for the kinetic energy released to matter. It is the kinetic energy of all charged particles **released** per unit mass [24]. The total kerma is usually divided into the collision and radiation kerma. K_{coll} is the energy released in collision type interactions like production of electrons by means of Coulomb interactions, while K_{rad} is the energy released in radiative interactions like the Bremsstrahlung produced by the secondary particles [18]. The total kerma can be expressed as $K = K_{col} + K_{rad}$, and is usually measured in Gy or J kg^{-1} .

The absorbed dose is usually referred to as dose, and it is the energy **absorbed** per unit mass, and it accounts for any ionizing radiation on any target [24]. It has the same units as kerma.

The MEDAPP source provides a mixed beam of neutrons and photons and both contribute to the total dose. Upon interaction of neutrons with the argon gas contained in the cavity, γ -photons are generated. An additional contribution to the dose is made by the secondary electrons that are generated as a consequence of the interaction between the incoming radiation and the argon gas.

2.4.2 Bragg-Gray Cavity Theory

The evaluation of the dose is performed in the argon gas located in the middle cavity of the chamber. Given the geometry of the chamber and the location of the gas in an inner cavity between the walls and the central electrode, the cavity can be considered as a Bragg-Gray cavity.

A Bragg-Gray cavity is the sensitive region of a dosimeter that provides, under two specific conditions, a useful equation that facilitates the assessment of the dose deposition to the gas located in that region of the ionization chamber. The conditions to be a Bragg-Gray cavity are the following [18]:

1. The cavity size is smaller than the range of the incoming particles, so the boundaries of the cavity are not treated as a perturbation
2. No particle is generated inside the cavity, so the production of secondary electrons does not influence the total dose

Holding these conditions true, the equation of the dose can be recalled as [13]:

$$D_{gas} = \frac{Q}{m} \frac{\bar{W}_{gas}}{e} \quad (2.7)$$

Here, m corresponds to the mass of the gas of the cavity and e is the fundamental electron charge. Q is the total charge of the cavity and \bar{W}_{gas} is the energy required to produce a pair of ions in the chamber gas and depends on the used gas and energy of the produced secondary or Δ electrons. Several values for \bar{W}_{gas} are listed on Table III on the *Protocol for Neutron Beam Dosimetry* [4].

2.4.3 Spencer-Attix Cavity Theory

In general, the Bragg-Gray conditions are not always met and the production of secondary electrons is not negligible. For this reason, several adjustments and corrections are applied to the theory to account for them. The Spencer-Attix theory is a more general solution that gives the dose of the gas in relation with the dose to the chamber wall and the effective mass stopping power of the wall to the gas [4]:

$$D_{wall} = S_{w,g} D_{gas} \quad (2.8)$$

Where $S_{w,g}$ is the effective mass stopping power ratio of the wall to gas, and D_{gas} is Equation 2.7. The cavity conditions are met depending on the cavity size, range of electrons and heavy ions in the cavity and the -secondary- electron energy. In general, they are met if the neutron beam has a high energy [18], which is the case that concerns the scenario of the ionization chamber under study.

If the gas of the cavity is substituted by a tissue of interest, consider a small chamber, a source of mixed γ and neutron radiation, the total dose of the tissue results in [18]:

$$D_{tissue} = \frac{Q}{m} \frac{\bar{W}_{gas}}{e} S_{tissue,gas} p_{fl} p_{dis} p_{wall} p_{cell} \quad (2.9)$$

In Equation 2.9, p_{fl} refers to the electron fluence perturbation correction factor, p_{dis} is the correction factor for displacement of the effective measurement point, p_{wall} is the wall correction factor and p_{cell} is the correction factor for the central electrode [18].

The factor p_{dis} depends on the on both the radiation quality and the dimensions of the gas cavity. According to IAEA TRSS 2777 and IAEA TRS 398 as discussed in 9.7.2 of [18], a recommended value for cylindrical chambers is 0.5 times the radius.

p_{wall} is added to the product to correct the perturbation of the wall of the chamber. Without this term, it would be assumed that the electron fluence of the sensitive region is the same without a wall.

The last factor p_{cell} corrects the slight increase in the signal due to the presence of the central electrode. This effect is found to be negligible for photons, yet relevant for neutron and electron beams.

Equation 2.9 gives the **total** dose of a mixed constant beam of neutrons and γ -photons irradiating the whole sensitive region of an ionization chamber approximated as a **Bragg-Gray** cavity and regarding the appropriate corrections mentioned.

The eventual difficulty to determine the correction parameters prevents from applying the above equations and leaves the application of the two chamber method as the only chance to measure the dose.

2.4.4 The Two Chamber Method

The two chamber method is a widely used technique in the field of fast neutron dosimetry. It is typically applied when the gamma component of the beam is strong, and is designed to separate the gamma and neutron components of the total dose. The method consists of using two ionization chambers of similar size, but with different gas and wall materials.

The first chamber, commonly referred to as the neutron-sensitive chamber, is specifically designed to have a very high sensitivity to both neutrons and photons.

Typically, the chamber's wall is made of a tissue-equivalent plastic material like A-150, while the cavity itself is filled with a tissue-equivalent gas. Its primary purpose is to quantify the neutron component of the overall radiation dose [18].

The second chamber, also known as the gamma-sensitive chamber, is designed to have a low sensitivity to neutrons and a high sensitivity to photons. The wall of this chamber is typically made of a material like magnesium, and the cavity is filled with argon gas [18].

The total dose measured for both chambers includes both the gamma and neutron components. By comparing the dose measured in the two chambers, it is possible to separate the gamma and neutron components and determine the total dose.

The two chamber method is applied when it is not possible to measure the neutron kerma. By using a response function $\alpha_{\gamma,cal}$, one can establish the next response equation for each chamber [18]:

$$D' = \alpha_{\gamma,cal} R_{total} = D'_n + D'_\gamma \quad (2.10)$$

The last terms, D'_n and D'_γ are the formal dose related to the neutron and photon components. Assuming that the ratio between the formal and actual dose is the same as the ratio of the sensitivities in the reference photon field [23], Equation 2.10 can also be expressed in terms of the actual dose as follows:

$$D' = \alpha_{\gamma,cal} R_{total} = kD_n + hD_\gamma \quad (2.11)$$

Being k and h the sensitivity response functions for the neutron and gamma components i.e $\frac{\alpha_{\gamma,cal}}{\alpha_n}$ and $\frac{\alpha_{\gamma,cal}}{\alpha_\gamma}$, respectively.

Thus, the next relationship can be established for the dose of each chamber as stated in Equation 2.12 and 2.13 [23]:

$$D'_U = k_U D_n + h_U D_\gamma \quad (2.12)$$

$$D'_T = k_T D_n + h_T D_\gamma \quad (2.13)$$

These two relations are the response functions of each ionization chamber under a field that combines neutron and gamma radiation. These are the equations that will be used to obtain the sensibility of the chamber during the calibration measurements at PTB.

2.5 Monte Carlo Simulation

The Monte Carlo method is a statistical technique used to simulate and analyze complex systems. The basic idea behind the Monte Carlo method is to use random

sampling to simulate complex probabilistic events [5]. This is done by generating numbers between 0 and 1 repeatedly in a computer, and those numbers are used to generate a distribution of samples that represent the target probability distribution [5].

The key advantage of the Monte Carlo method is that it can be used to analyze systems that are cannot be solved using deterministic methods. It can be used, for instance, to predict the response of a system of particles that account for interactions with each other. These interactions are particle collisions and inherently stochastic.

The Monte Carlo method can be applied to a wide variety of problems whose nature is in a good fit for the method. To predict the response of a particle system that accounts for nuclear reactions, one of the most powerful applications is the Monte Carlo N-Particle simulation (MCNP). An overview of MCNP simulation will be provided below.

2.5.1 MCNP Simulations

MCNP is a general-purpose radiation-transport code whose purpose is to solve a particle transport problem in a simulated environment using the Monte Carlo method. [28]

The code is developed and maintained by Los Alamos National Laboratory in Los Alamos, New Mexico (USA). One of the many applications of the code is dosimetry. In this field, generally a detailed environment is created and loaded into the code via input file. The configuration of the simulation is established in the input file using a set of cards for each element that is to be present in the environment. MCNP offers a card for every feature of the simulation regarding the physics of the problem or the geometrical setup. The input of MCNP is then, a simple text file that includes the cards and geometric boundaries organized in three code blocks, as it is required by the code engine. The execution takes place in the command line and the only graphic interface if only meant to visualise the geometry.

MCNP allows the user to freely set up the materials and the structures simulated. The structures are built defining planes in a Cartesian system and forming volumes out of their intersections. In the simulations of this project, it has been followed the definition, molecular fraction and cross section listed on the *Compendium of Material Composition Data for Radiation Transport Modeling* [20]. The compendium has undergone several revisions year by year and it contains today the most up to date and tailored information of the material composition for MCNP problems.

An important card used in the analysis performed in the next chapters is the tally card. Tallies can be thought of as detectors placed within a cell to measure the desired quantity. For example, the neutron and charge flux can be calculated and graphically displayed. The dose disposition tally $F6$, is perhaps the most relevant in the problem of the ionization chamber.

The output of MCP6 is another text file containing all the value of the quantity

measured with each tally. The result for the $F6$ tally is provided in MeV g^{-1} by default, and the particle flux in number of particles per square centimeter [29]. Every measurement comes along with its statistical error.

In some cases, it is necessary to extract the output data of MCNP and handle them with a more powerful data treatment software to be able to perform a decent analysis of the problem. This is the case of the ionization chamber simulations. Here, the simulation has been executed multiple times in an automated application in Python, each in a slightly changed environment, to study the response of the device.

3 Atmospheric Corrosion of Mg

Magnesium is the material used to build the outer wall of the PTW TM33054 chamber. It is a suitable material to build ionization chambers because it has a low interaction with neutrons. However, magnesium is very prone to corrosion when it comes into contact with other elements present in the atmosphere. Corrosion is a chemical reaction whose products remain on the surface of the metal where it takes place. In the case of the magnesium chambers, the products are deposited over the internal and external side of the magnesium wall.

The products have an unknown composition, and they might eventually interact with the radiation that reaches the detector. For this reason, this chapter explores the hypothesis that the interaction of corrosion products can affect the dose measurement of the ionization chamber. Furthermore, this chapter presents evidence supporting the presence of corrosion products.

To investigate this hypothesis, a simulation of the chamber is conducted, including different concentrations of corrosion product layers. The goal here is to compare and understand how the corrosion affects the dose deposition in the sensitive region when the MEDAPP source is applied.

Additional context regarding the corrosion of the PTW TM33054 ionization chamber is provided in the following subsection. The information provided relies in the doctoral work of Martin Jönsson done at the KTH Royal Institute of Technology in Stockholm, Sweden.

3.1 Corrosion of Ionization Chambers

Magnesium is a reactive material that tends to donate electrons in chemical reactions. In environments with higher moisture levels, magnesium is more likely to undergo oxidation.

A series of oxidation and reduction reactions occur when magnesium reacts with the water and oxygen present in the atmosphere. These reactions produce numerous hydroxide ions, OH^- , that give rise to corrosion products.

Martin Jönsson's study is focused on the influence of the microstructure and environment of magnesium alloys. It is demonstrated in his work that the initial corrosion product formed immediately after the oxidation reaction is magnesium hydroxide, $Mg(OH)_2$. After several days of exposure to the same temperature and humidity conditions, the final compound found on the alloy surface is **hydromagnesite** [14].

In his work it is concluded that the microstructure of the alloy plays a fundamental role in the corrosion behaviour as well as the presence of $NaCl$ in the air. The conditions that apply to the ionization chambers exclude any amount of sodium chloride that could accelerate the corrosion reactions. The relative humidity of the atmosphere of FRM II is lower than in the location where Martin Jönnsen's research was conducted and the wall of the chamber is made of pure magnesium. Therefore, the corrosion rate of the magnesium, and hence the thickness of the layer, is expected to be lower in the chambers than in the alloys assessed in his work, which is about a few micrometers per year.

While it may not be feasible to identify the corrosion material of the PTW chambers using imaging techniques, the next section demonstrates the presence of a corrosion layer through neutron imaging. Furthermore, an estimation of the layer thickness is provided, which will be utilized in the coming MCNP simulations.

3.2 X-Ray and Neutron Imaging

Several CT scans have been run to search for a corrosion layer. Additionally, another scan has been run using thermal neutrons to compare both results. The result is shown for the EXRADIN and PTW chambers in Figure 3.1.

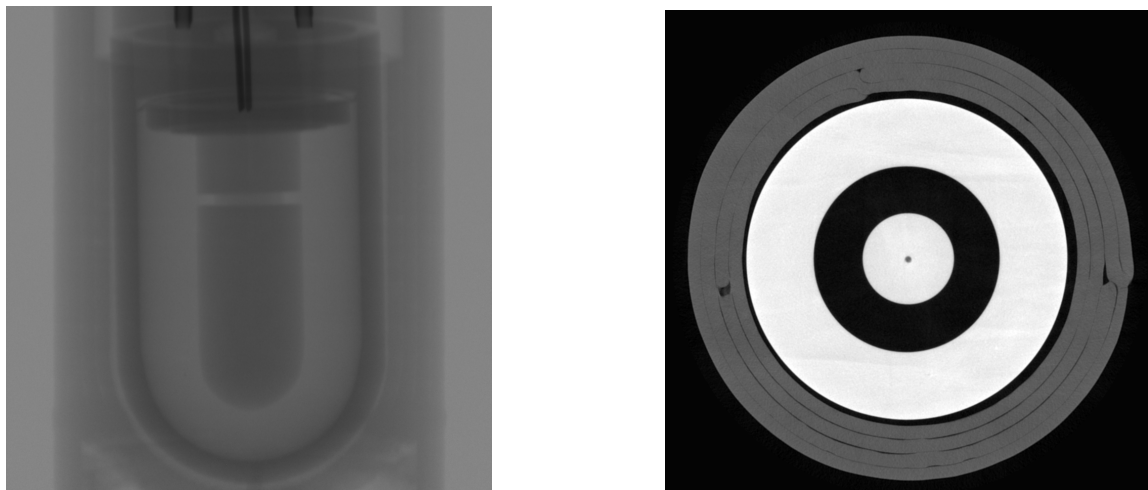


Figure 3.1: X-ray CT scan of EXRADIN chamber (left) and the PTW TM33054 chamber (right). Both devices are made of magnesium.

The inner structure is shown in both images. There are several flaws in the material that can be seen on the scan. There are small air bubbles in the center of the chamber as of the black color that represents the air.

As illustrated in the next image, small bubbles are also allocated within the magnesium structure (the white region):



Figure 3.2: Image of the X-ray CT scan of the PTW TM33054 ionization chamber.

The same imperfections in the materials appear in the successive images taken along the axial direction of the chamber. However, there are no evidences of corrosion over the surfaces in any of the images. This fact can be attributed to the null interaction of the corrosion with photons.

Since neutrons interact differently with the chamber, the outcome of the neutron scan reveals that the surface of the magnesium wall is covered with a different composite. In Figure 3.3, the neutron scan of the PTW TM33054 magnesium chamber is represented along with a plot of the gray values against the width of the chamber. The distances of the plot have been scaled to the actual size of the chamber.

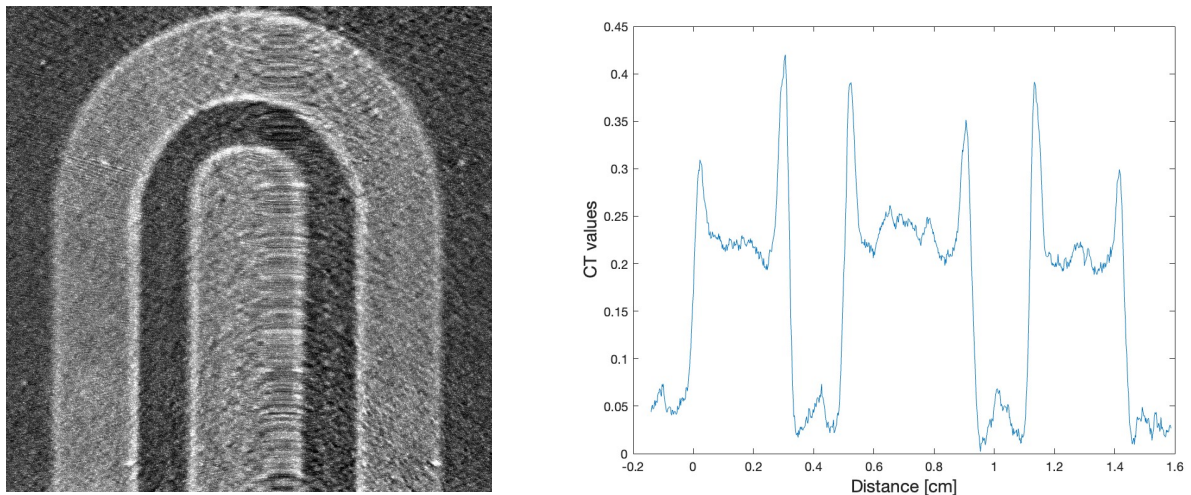


Figure 3.3: Neutron scan of TM33054 (left) and CT values vs. distance plot (right).

The total thickness of the chamber is 1.4 cm, according to *PTW Freiburg, Ionization chambers for neutron dosimetry* [16]. In the plot of Figure 3.3, the CT signal appears beyond the boundaries of the chamber. This is because the signal of the air around the chamber has also been plotted for statistical purposes. Even though the oxidation material is visible, it is not possible to identify its composition from neutron scan. However, the thickness can be **estimated**.

The CT values peak at the boundaries of the magnesium wall and the central anode with the surrounding environment. For each peak, the FWHM has been measured digitally. The full width half maximum provides the width of the CT value signal, which is, in the context of this neutron scan, the same as the layer.

The final result has been averaged over all peaks. This average result is equal to:

$$0.37 \pm 0.02 \text{ mm} \quad (3.1)$$

3.3 Simulated Oxidation Layers

The results exposed here are for the PTW TM33054 magnesium chamber with a layer of **hydromagnesite** on all the magnesium surfaces. In this section, it is intended to study the differences in the response when a layer of corrosion of the mentioned composite is present. For this purpose, the MCNP simulation tally the dose absorbed by the argon gas. The simulations have been conducted using the geometry setup of Figure 3.4:

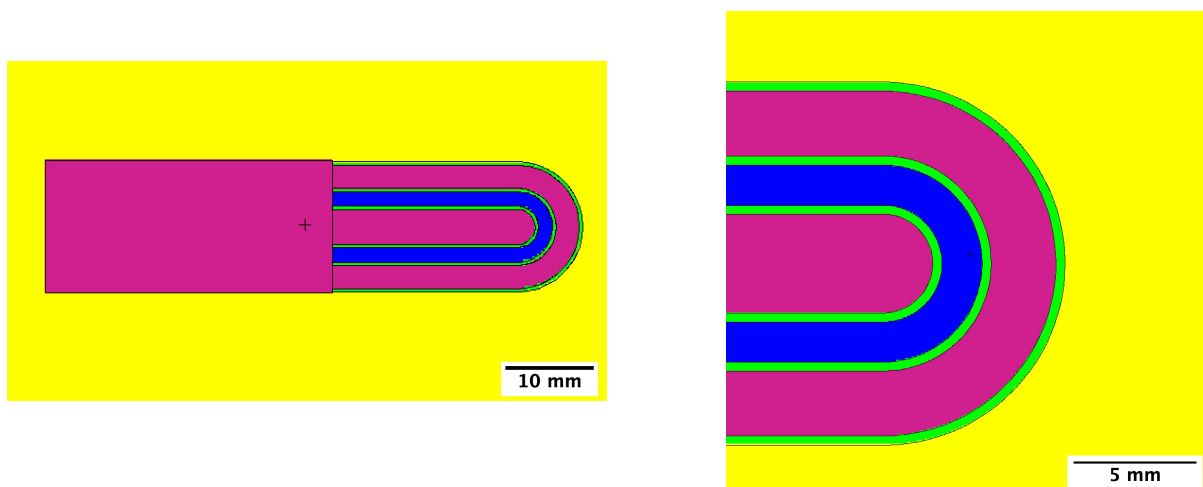


Figure 3.4: Simulated PTW chamber (left) and a close-up of the tip of the chamber (right). In the close-up, it is noticeable that a layer of hydromagnesite, shown in green, is added to the surface of the anode and to the inner part of the wall. The scale bar has been placed at the bottom of both images.

In the simulation that includes the corrosion layer, the source of radiation is the MEDAPP source. The simulation is also run using the same source, but removing the photon contribution. The purpose of it is to compare the response of the device without the influence of gamma radiation.

The density of argon is, according to the *National Institute of Standards and Technology* [1], equal to 1.66 mg cm^{-3} . For hydromagnesite, the average density is 2.18 g cm^{-3} according to the *Mineralogy Database* [2]. Furthermore, the simulation also runs with a material that is a mixture of hydromagnesite and a small amount of water. This is done to consider the case in which a certain amount of atmospheric water is dissolved into the hydromagnesite. The high interaction probability of neutrons with hydrogen can significantly affect the reading of the chamber. Therefore, it is of interest to consider this case as well. In MCNP, the mixed material of hydromagnesite and water has been simulated by calculating respectively the molecular fraction of each element according to the desired concentration of water. The molecular weight that is used to calculate the molecular fraction when the mineral is mixed with water is also taken from the database [2].

3.3.1 MEDAPP Source with a Hydromagnesite Corrosion Layer

The source of radiation used in this simulation is the **MEDAPP** source accounting for the contribution of **neutrons and photons** and the total number of particles simulated is 10^8 . The reason for this decision is the trade-off between the computational time and the statistical error of the results: while a higher number of particles will sharpen-up the results, it will slow down the execution dramatically beyond 10^8 particles. Finally, the **thickness** has been set to **0.37 mm**. The density of hydromagnesite decreases slightly as the fraction of water increases. This has been taken into account in the simulation and the density has been set according to the next table for each case:

% of water	Density [g cm^{-3}]
0	2.18
1	2.17
2	2.16
3	2.14

Table 3.1: Density of the hydromagnesite composite accounting for a percentage of water.

Figure 3.5 shows the tally +F6, which accounts for the total dose deposited by all particles, against the density of the argon gas. The same tally **without** any corrosion layer is included in the same figure to compare.

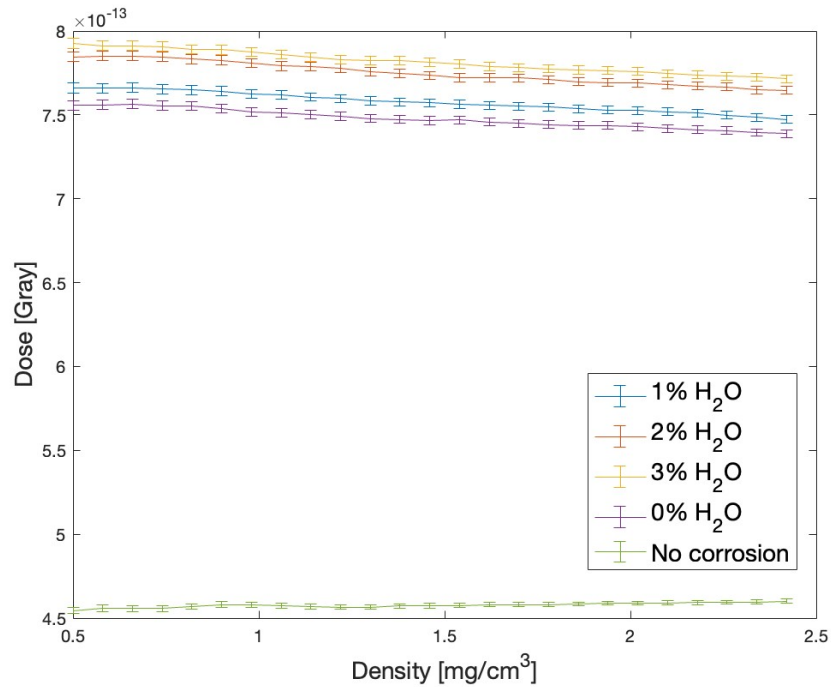


Figure 3.5: Simulation of PTW TM33054 with a 0.37 mm thick layer of hydromagnesite on all magnesium surfaces. Tally +F6. In the legend the fraction of water is stated in percentages.

From the graph, it is evident that as the density of argon increases, there is a general downward trend in the deposited dose. Here, the downward trend is caused due to the increase of total mass in the sensitive region since the relationship between dose and mass is $D = \frac{E}{m}$, where D is the dose, E the energy and m the mass of the gas. The presence of a higher concentration of water in the layer leads to a greater generation of secondary protons and hence to a deposition of dose.

The energy deposited in the sensitive region where the argon gas is located is a measure of interest. To come up with that plot, the energy deposition is calculated as *Dose x mass*, where the dose is in MeV and the mass is the mass of the argon in g, which has been calculated by $\rho \times V$. The density ρ is the density of the gas in g, and the volume V has been read from MCNP as 0.79 cm^3 . The total energy deposition is, then:

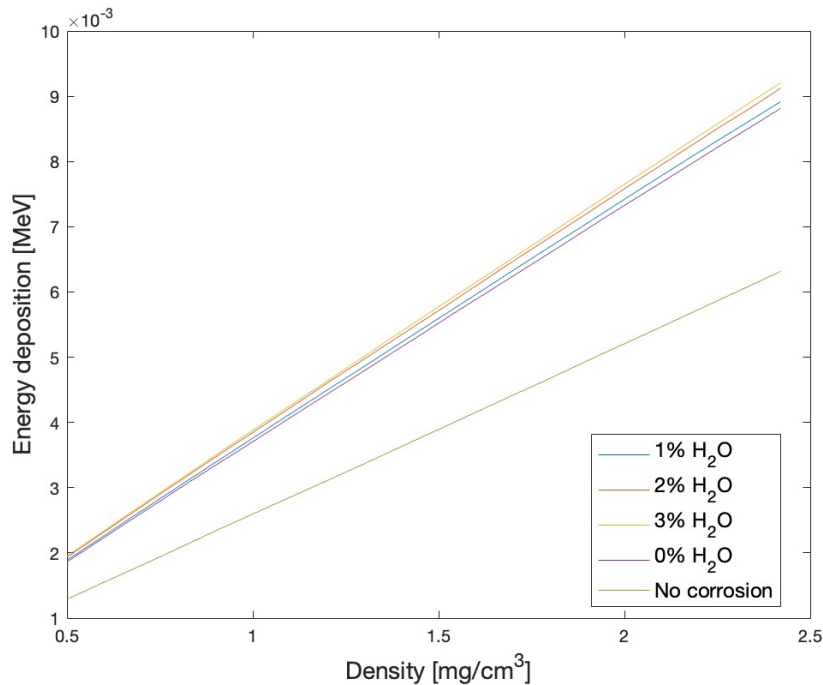


Figure 3.6: Energy deposition in the sensitive region of the PTW TM33054 chamber with a hydromagnesite layer.

The relationship between the argon mass and the density is linear. Therefore, the **total** energy deposition shows an increasing trend.

To compare the energy absorption further, the data presented in the Figure 3.6 are fitted linearly and the slope of each function is calculated. In the next table, the slopes are presented for each simulation:

% of water	Slope [10^{-3}]
No corrosion	2.6
0	3.6
1	3.7
2	3.7
3	3.8

Table 3.2: Slope comparison of the linear fit for the energy deposition of the MEDAPP source in PTW TM33054. No corrosion corresponds to the simulation of the chamber where no corrosion layer has been included.

The slope increases between 1 and 4 % per fraction of water. The minimum increase of slope with regards to the simulation without a corrosion layer is more than 20 %. In this result it is shown that the presence of a corrosion layer does influence the absorbed dose, although it is not necessary for the gas to absorb any amount of the energy.

Following the energy deposition, the contribution of the **neutrons** to the total dose is:

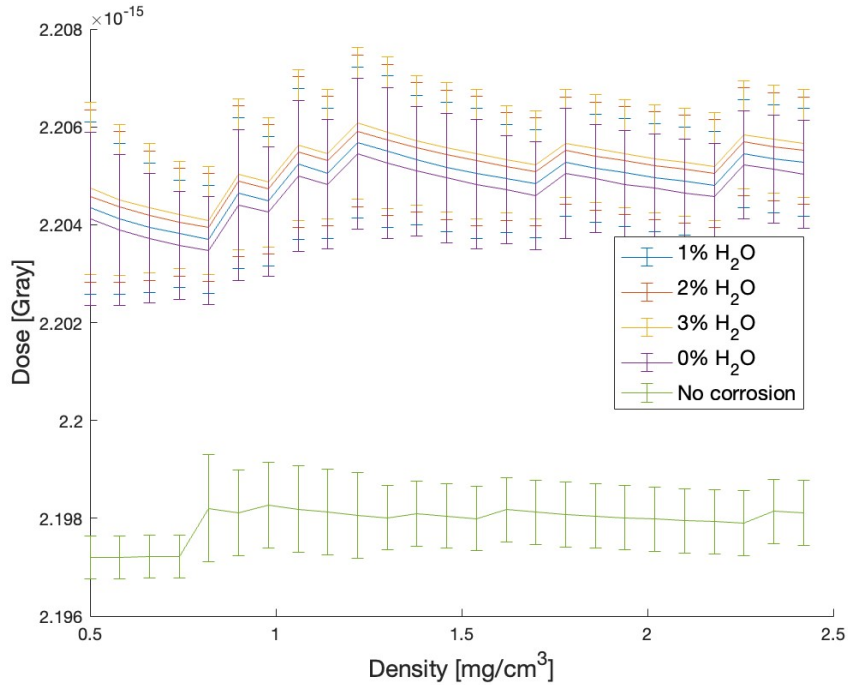


Figure 3.7: Dose delivered by neutrons in the sensitive region of the PTW TM33054 chamber with a 0.37 mm thick hydromagnesite layer.

The neutron contribution is perhaps one of the lowest of this simulation. The value barely changes with the fraction of water. However, the dose deposited is about 1% lower in the case of the simulation where no corrosion layer has been included. With a dose of the order of $2.2 \cdot 10^{-15}$ Gy in presence of corrosion, it is lower than the dose delivered by electrons and photons by a factor of 100, which is presented up next in Figure 3.8.

Electrons and protons contribute to the dose as follows:

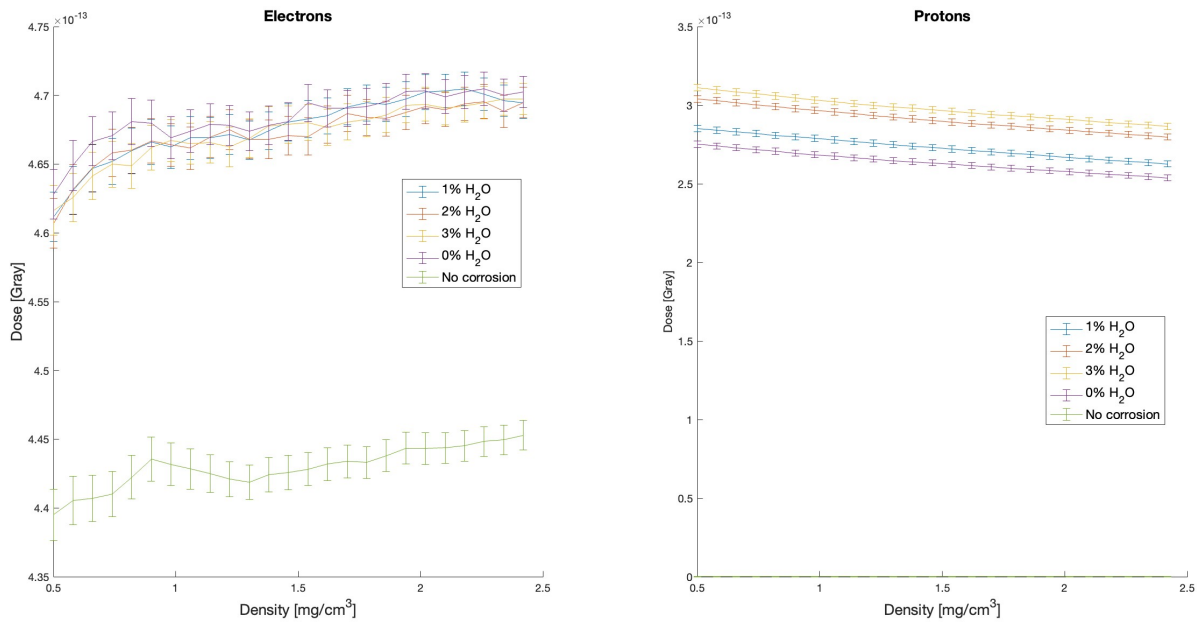


Figure 3.8: Simulation of PTW TM33054 with a 0.37 mm thick layer of hydromagnesite on all magnesium surfaces. Electron and proton contribution.

Although the lines of the dose for the respective fractions of water appear in the subplots very close to each other (except in the total and proton plot), the sensitive region's behaviour is the same for all kinds of particles except for electrons. Electrons slightly depend on the fraction of water as they show a variation of roughly 1 % of the dose delivered. Protons, on the other hand, happen to be more relevant as their dose deposition varies about 5 % across the fractions of water

However, photons and heavy ions do not play a role in the dose and their contribution is of the order of 10^{-13} and 10^{-14} Gy, respectively. For this reason, their plots are not shown here.

3.3.2 Neutron Source with a Hydromagnesite Corrosion Layer

In this simulation, the contribution of the photons is excluded in MCNP. The source only has the neutron contribution. The number of particles and the thickness of the layer is the same as in the previous simulation. For the neutrons, the energy and probability distribution is exactly the same as in the previous case. The total dose delivered by the source in the sensitive region is plotted in Figure 3.9.

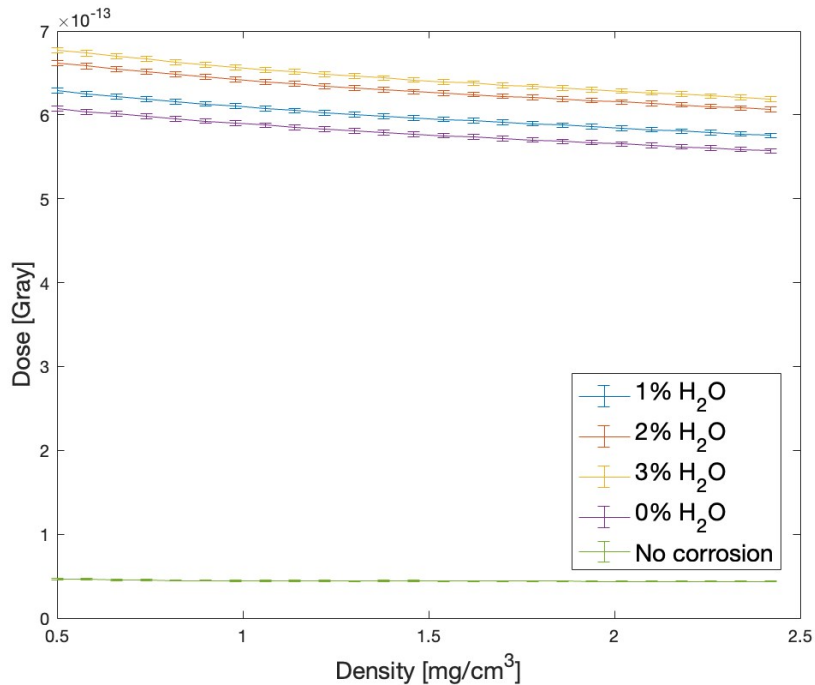


Figure 3.9: Simulation of PTW TM33054 with a 0.37 mm thick layer of hydromagnesite on all magnesium surfaces using the MEDAPP neutron source. Tally +F6. In the legend the fraction of water is stated in percentages.

The dose is slightly lower in this simulation because of the lack of photons, which also deliver a certain dose and generate secondary particles. The dose delivered in the simulation that has no corrosion layer is notably lower than the rest. The total dose absorbed by the gas in that simulation is about 90 % lower in absence of photons. This means that neutrons barely interact with the magnesium outer layer, while they do with the hydrogen atoms present in the corrosion layer. Thus, the layer does play a significant role when only neutrons are used as a source.

The total en energy deposition is also calculated in this simulation and is plotted in Figure 3.10.

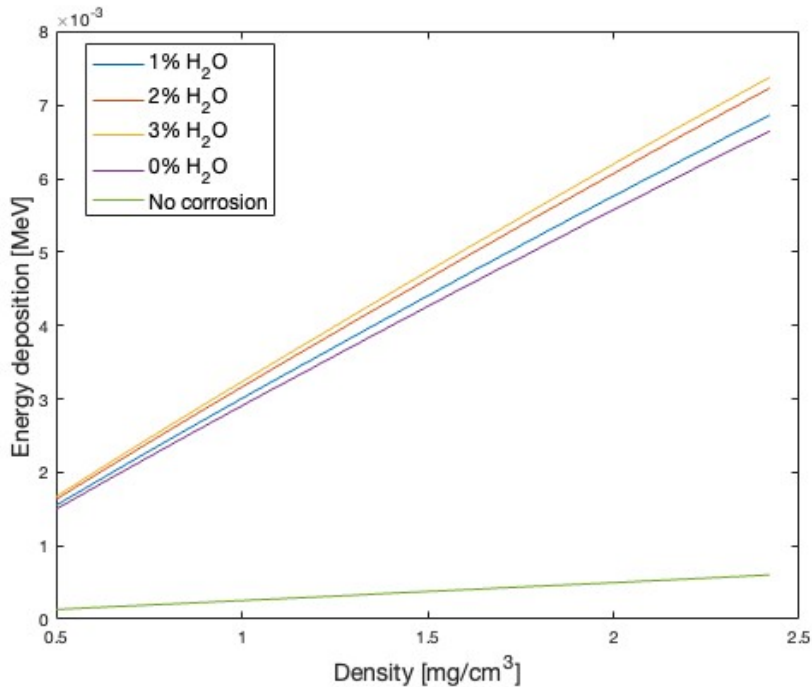


Figure 3.10: Energy deposition in the sensitive region of the PTW TM33054 chamber with a hydromagnesite layer using the MEDAPP neutron source.

As presented the simulation using the complete MEDAPP source, a comparison of the energy absorption for the fractions of water is made using a linear fit. In the next table, the slopes are presented for each simulation:

% of water	Slope [10^{-3}]
No corrosion	0.24
0	2.7
1	2.8
2	2.9
3	3.0

Table 3.3: Slope comparison of the linear fit for the energy deposition of the MEDAPP neutron source in PTW TM33054. No corrosion corresponds to the simulation of the chamber where no corrosion layer is included.

Again, the slope increases between 1 and 4 % per fraction of water. As suggested before, the most significant contrast is observed in the simulation without corrosion, where the slope is about 97 % lower than in the presence of the layer. The presence of the layer can be regarded as necessary in the case of a neutron source for the chamber

to absorb a significant dose. The contribution of the neutrons, electrons and protons is presented next:

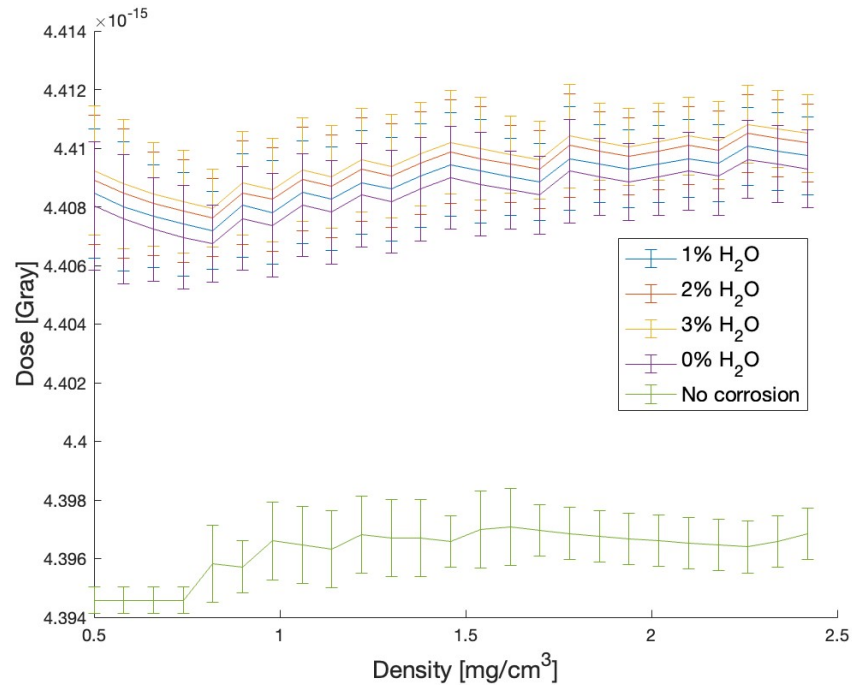


Figure 3.11: Simulation of PTW TM33054 with a 0.37 mm thick layer of hydromagnesite on all magnesium surfaces using the MEDAPP neutron source. Neutron contribution.

As it is expected, the neutron contribution is almost twice as strong as the complete MEDAPP source, in which the chamber is irradiated only with neutrons.

The electron and proton contribution is shown in the next plot:

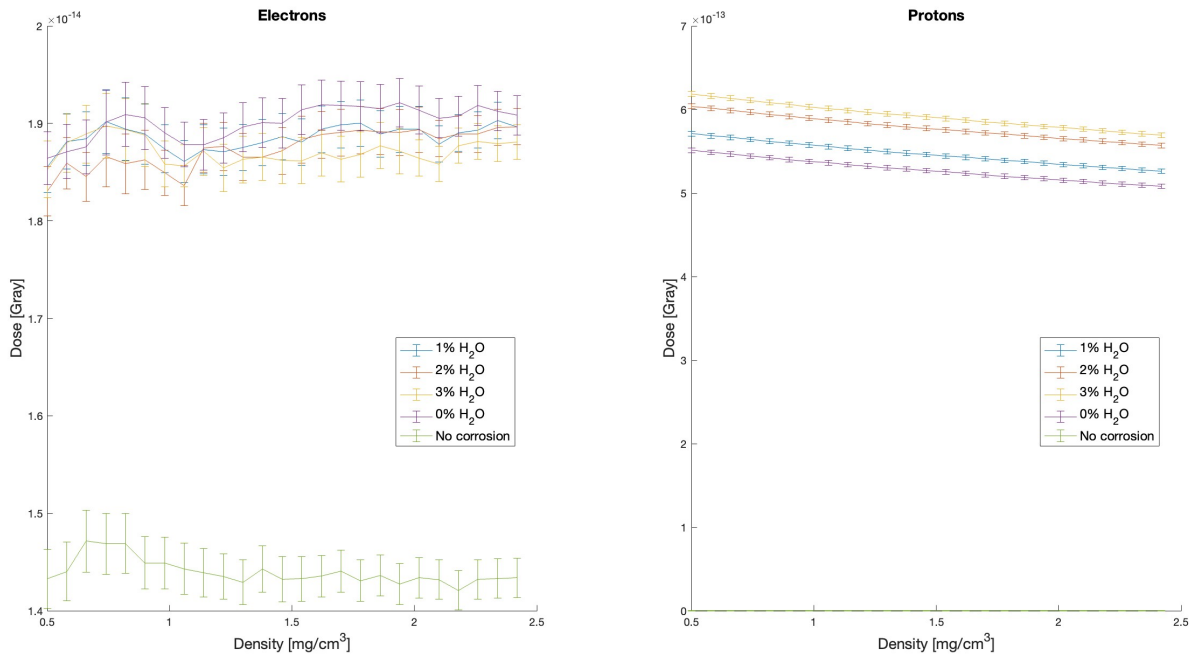


Figure 3.12: Simulation of PTW TM33054 with a 0.37 mm thick layer of hydromagnesite on all magnesium surfaces. Electron and proton contribution.

There are almost no protons generated by the neutron source when there is no corrosion layer. The dose of that simulation is of the order of 10^{-17} Gy.

4 Reference Measurements

4.1 Calibration Measurements in Neutron Reference Field

Several ionization chambers have been calibrated at the National Metrology Institute of Germany (PTB). To carry out the calibration measurements on the chambers, a pure neutron field of quasi monoenergetic neutrons has been used to irradiate the chambers at different energies. Even though the source does not have the same energy configuration as the MEDAPP, it does generate fast neutrons at the same energy of the MEDAPP facilities. For this reason, the PTB facilities have been found to be suitable for the calibration of the devices.

It is intended in this subsection to calculate the sensibility of the chamber. To calculate it for the PTW chambers TE-13 TM33053, TE-14 TM33053 and Mg-01 TM33054, respectively, the following formula is applied [22]:

$$k_{T,U} = \frac{k_a G_{aw} V_{LG} k_f Q}{KERMA} \quad (4.1)$$

In Equation 4.1, k_a is the chamber specific air kerma calibration value, G_{aw} is the k_a effective dose conversion factor, V_{LG} is the correction factor for the air-gas measurement, k_f is the environmental correction factor for the pressure and temperature of the air and Q is the accumulated charge in the ionization chamber. The constants used in Equation 4.1 are in Table 4.1. The environmental correction factor k_f has been calculated using Equation 4.2:

$$k_f = \frac{P_0 T}{P T_0} \quad (4.2)$$

where P_0 and T_0 are reference pressure and temperature values. The constant values are specific for each chamber type. A summary of the values used in the calculations is to be found in Table 4.1.

The temperature and atmospheric pressure have been measured for every measurement of the charge. The value of KERMA is the dose absorbed by the chamber and it has been measured to be between 5.4 and 5.6 mGy, depending on the device. To take the measurements, each device has been positioned at the center of a platform as shown in Figure 4.1 and it has been irradiated by the neutron source perpendicularly.

P_0 [mbar]	1013.25
T_0 [K]	293.2
G_{aw}	1.112
V_{LG} (TE-13/14)	0.861
K_a (TE-13)[Gy C $^{-1}$]	$3.10 \cdot 10^7$
K_a (TE-14)[Gy C $^{-1}$]	$3.09 \cdot 10^7$
V_{LG} (Mg-01)	0.688
K_a (Mg-01)[Gy C $^{-1}$]	$2.68 \cdot 10^7$

Table 4.1: Constants used in Equation 4.1.



Figure 4.1: Picture of a ionization chamber set up at PTB Braunschweig. The chamber is located in the middle and set up vertically. On the right side, the radiation source is pointing perpendicularly to the tip of the chamber.

The temperature and atmospheric pressure have been measured once for each energy. The values are in the range of 20.07 and 21.7 °C, and 996.9 and 1001.9 mbar. The correction factor associated to this parameters, k_f , is around 1.01. For the energies 1.2 and 2.5 MeV, the kerma values, $k_{T,U}$ of each chamber have been calculated. The calculated k_T and k_U for the PTW chambers is:

1.2 MeV				
	Chamber	Charge [pC]	KERMA [mGy]	k_T
PTW	TE-14	173.60	5.6	0.932 ± 0.001
		176.80	5.6	0.950 ± 0.001
		177.40	5.6	0.953 ± 0.001
	TE-13	183.80	5.6	0.984 ± 0.001
		183.30	5.6	0.982 ± 0.001
		183.20	5.6	0.981 ± 0.001
	Chamber	Charge [pC]	KERMA [mGy]	k_U
PTW	Mg-01	72.59	5.6	0.269 ± 0.001
		73.37	5.6	0.272 ± 0.001
		72.72	5.6	0.269 ± 0.001

Table 4.2: Calculated k_T and k_U for the PTW tissue equivalent and magnesium chambers at 1.2 MeV, respectively.

2.5 MeV				
	Chamber	Charge [pC]	KERMA [mGy]	k_T
PTW	TE-14	185.6	5.4	1.029 ± 0.001
		186.2	5.4	1.033 ± 0.001
		186.1	5.4	1.032 ± 0.001
	TE-13	186.2	5.4	1.038 ± 0.001
		186.6	5.4	1.040 ± 0.001
		186.1	5.6	1.037 ± 0.001
	Chamber	Charge [pC]	KERMA [mGy]	k_U
PTW	Mg-01	52.54	5.4	0.202 ± 0.001
		52.41	5.4	0.202 ± 0.001
		52.41	5.4	0.202 ± 0.001

Table 4.3: Calculated k_T and k_U for the PTW tissue equivalent and magnesium chambers at 2.5 MeV, respectively.

4.1.1 Data Comparison

The same measurements were performed by the MEDAPP team at the same facility for the same ionization chambers in 2018. According to the calibration performed by Dr. Markus Kellermeier and Dr. Lucas Sommer [22], the values of the measured kerma have varied at 2.5 MeV with regards to those stated on the report.

A comparison of the values of the sensibility for the ionization chamber is presented. The values of k_U and k_T are calculated from the initial measurements of the charge and KERMA of the calibration of 2018 [22] and are plotted in the next figure:

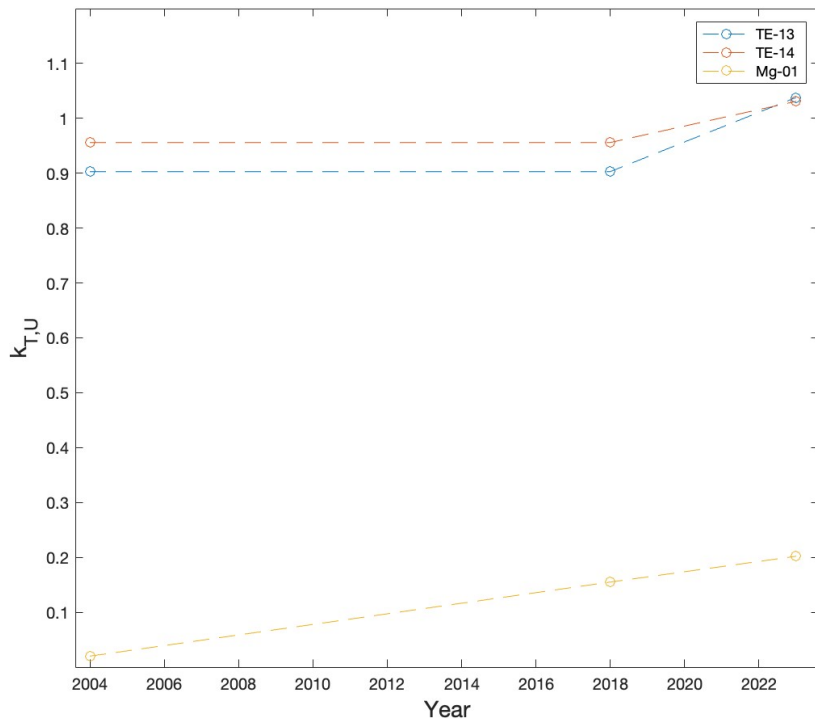


Figure 4.2: Values of k_U and k_T measured at PTB in different years for 2.5 MeV.

The sensibility in 2004 is taken from *Bericht zur Basisdosimetrie für medizinische Bestrahlung an der Strahlkonverteranlage am FRM-II Garching (2006)* [25] as 0.943 for TE-13 and TE-14 and assumed to be unchanged in 2018. For Mg-01, the value in 2004 is 0.02 [25]. A linear fit is also performed from the data of the Figure 4.2 in order to compare the slopes:

Chamber	Slope [10^{-3}]
TE-13	5.6
TE-14	3.1
Mg-01	9.6

Table 4.4: Slope comparison of the linear fit for the sensibility of the chambers TE-13, TE-14 and Mg-01 at 2.5 MeV.

In this comparison, TE-13 and TE-14 show similar and relatively higher slopes, between $3.1 \cdot 10^{-3}$ and $5.6 \cdot 10^{-3}$ [year] $^{-1}$, implying a consistent increase in sensibility over the measured period. On the other hand, Mg-01 has a lower slope of $9.6 \cdot 10^{-3}$ [year] $^{-1}$, indicating a less pronounced change in sensibility compared to the tissue equivalent chambers.

4.2 Build-up Effect

As neutrons slow down i.e. lose energy, the likelihood of interacting with atomic nuclei rises, resulting in a region near the material surface known as the "build-up region" of the material where neutron fluence increases significantly. In the next plot, that behaviour is clearly noticeable. In Figure 4.3, the cross section of neutrons is assessed on selected isotopes and hydrogen-rich plastic foils [10].

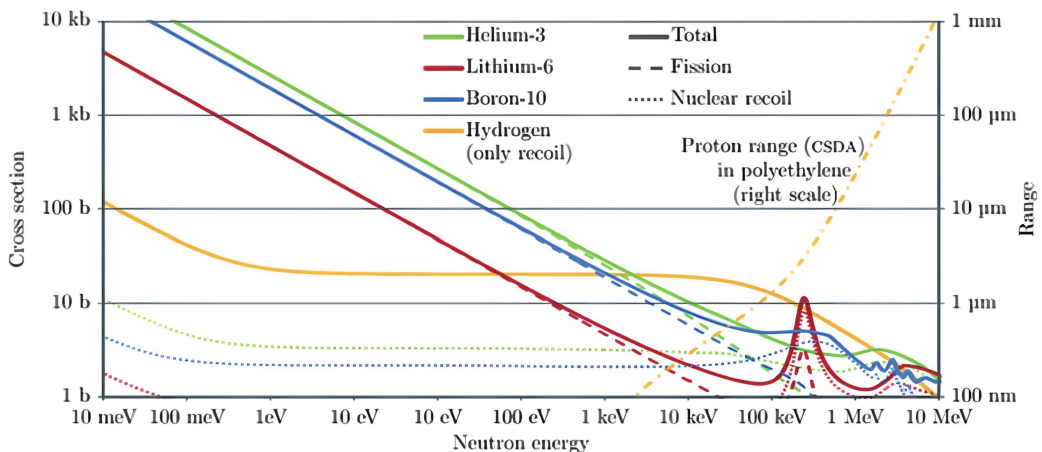


Figure 4.3: Cross section measured in *barns* of various selected isotopes as a function of neutron energy.

There are definite regions in Figure 4.3 where the cross section peaks at a certain value or experiments slight increase (depending on the target nuclei) to finally descend again at a higher neutron temperature. When this happens, the energy deposited in the material undergoes a fluctuation. This is the *build-up effect* and it might take place in both magnesium and tissue equivalent plastic ionization chambers. In this section,

the simulation of the effect in both materials is presented. In order to study it, the simulations are designed using a cylinder whose radius is 0.75 mm, and the energy deposition per cubic centimeter at different energies is measured. Finally, the source used in the simulations is a monochromatic plane neutron, as it was used at PTB.

4.2.1 Build-up Effect in Tissue Equivalent Plastic A-150 (TE)

With a density of 1.27 g cm^{-3} according to the *ESTAR Database* [1], the plastic shows a clear build-up effect that becomes more notable as the energy of the incoming beam rises. Using the **plane neutron source**, the tissue equivalent cylinder behaves as follows:

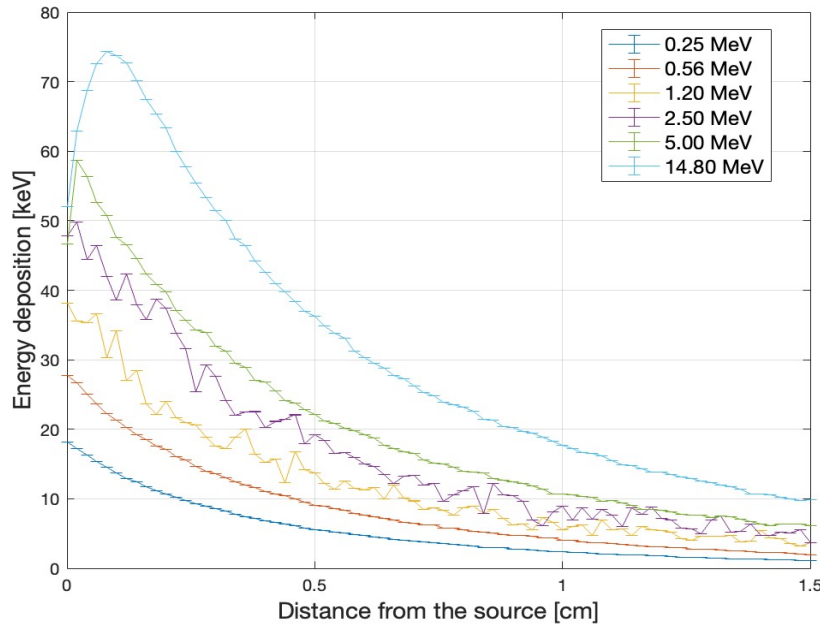


Figure 4.4: Energy deposition plot of a TE cylinder using a plane neutron source at different energies. There is no gap between the source plane and the cylinder.

Here, neutrons are primarily scattered by the constituent nuclei. As these neutrons travel deeper into the material, they engage in numerous interactions, transferring energy to atomic nuclei and generating secondary charged particles. This chain of interactions results in an increased dose deposition within the plastic at greater depths, which explains the slight displacement of the peak of energy deposition to the right as the energy of the beam increases, giving rise to the buildup effect that is observed beyond the energy of 2.5 MeV.

4.2.2 Build-up Effect in Magnesium

In this simulation, the same configuration for the neutron source as in the case of the TE material is used. The deposited energy in the magnesium cylinder is:

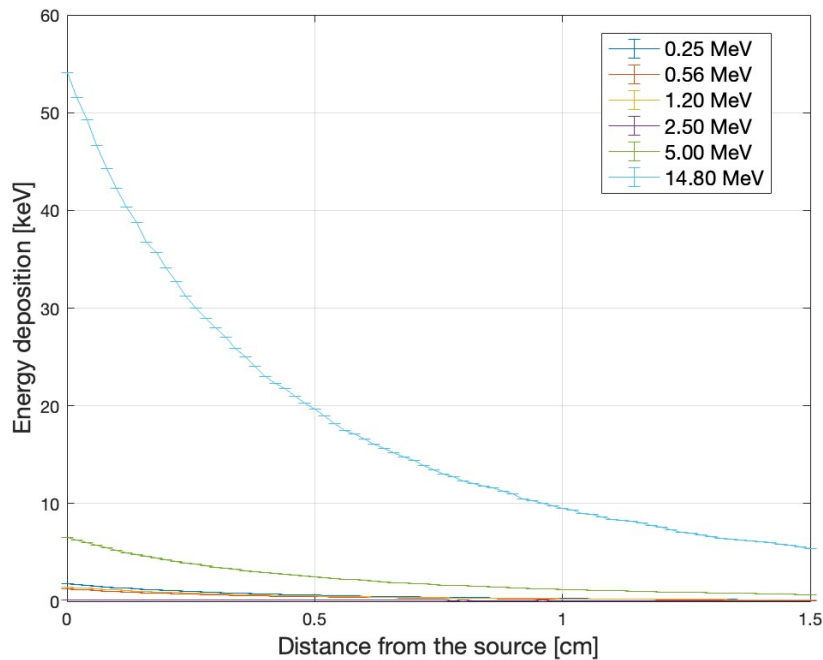


Figure 4.5: Energy deposition plot of the magnesium cylinder using a plane neutron source at different energies. There is no gap between the source plane and the cylinder.

According to the plot on Figure 4.5, there is apparently no build-up effect in this material. The difference between the energy deposition for the highest energy and the lower is too big to notice the response of the cylinder properly. For this reason, a close-up to the lowest energies is provided in the next plot:

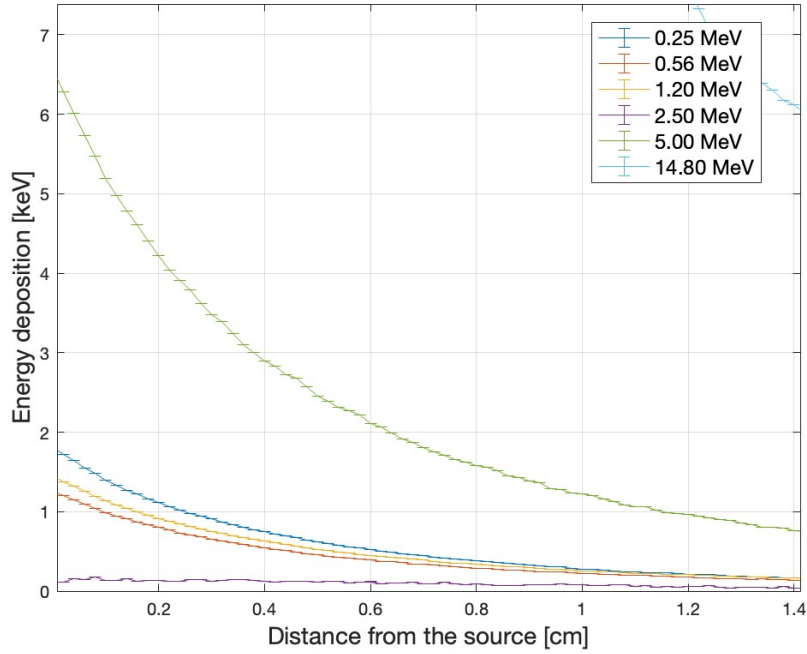


Figure 4.6: Close-up of the energy deposition plot of the magnesium cylinder plot using a plane neutron source at different energies. There is no gap between the source plane and the cylinder.

The lines of the energies 0.25 and 2.5 MeV appear to be switched, while the expected result should be a directly proportional relationship between the energy of the beam and the energy deposition. This behaviour is due to the neutrons hitting the nuclei at a **resonance** energy for which the cross section of the atom grows significantly. In order to confirm that, the cross section of the magnesium against the energy of the incident neutron is plotted next:

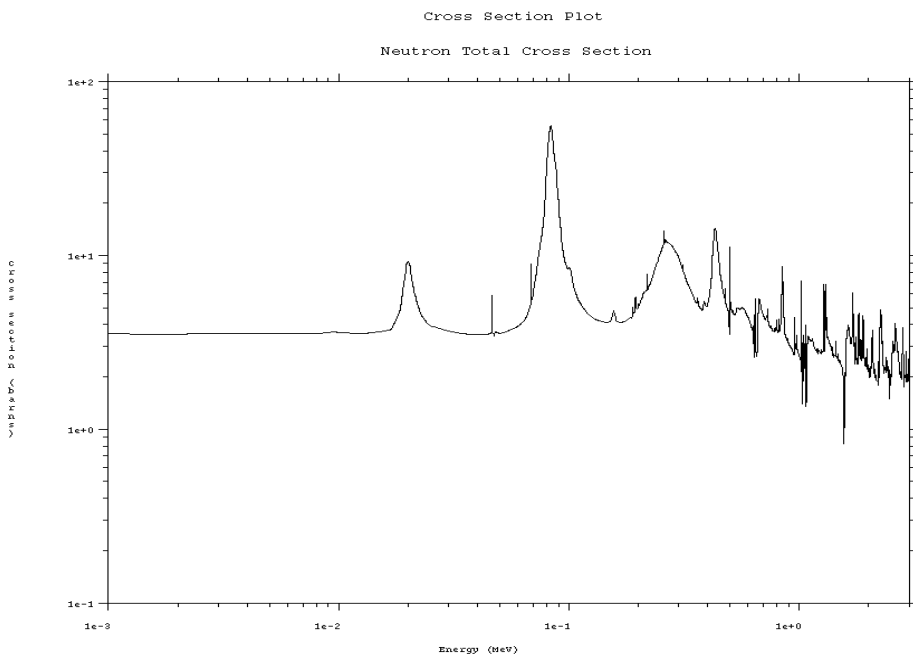


Figure 4.7: MCNP plot of the cross section in *barns* of Mg.

MCNP gives out the plots of the cross section of a material always in logarithmic scale. In this case, there is a sudden increase in the cross section for the energy of 0.25 MeV and, for that value of the energy, the cross section is higher than for the case of 2.5 MeV, which causes the plot in MCNP to show the energy deposition lines switched.

5 Simulated Check Source

5.1 ^{90}Sr as a Source

At MEDAPP, a sample of strontium-90 is used mainly as a β^- check source. It is chosen because the radiation spectrum is comparable to the MEDAPP spectrum and can produce comparable results when it irradiates an ionization chamber. The goal of this chapter is to model the β^- check source in MCNP to run a simulation on the PTW magnesium chamber TM33053 to study the effect of the corrosion layer.

As the strontium-90 decays it forms ^{39}Y and emits a β^- particle of 0.546 MeV [7] and this ^{39}Y , in turn, decays into ^{90}Zr emitting also a β^- particle of 2.274 MeV [7] according to the scheme:

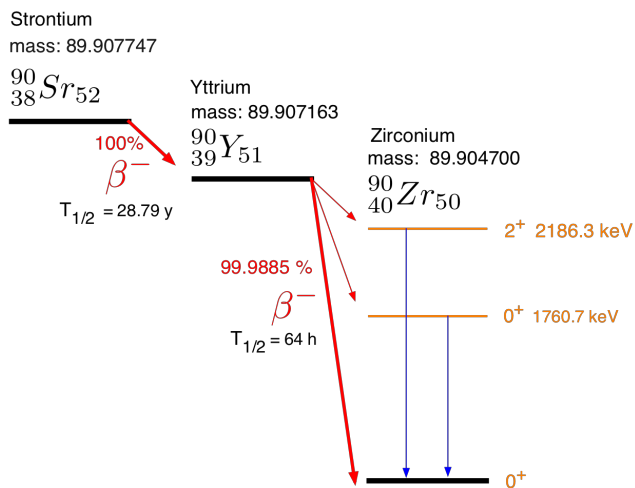


Figure 5.1: Decay scheme of Sr-90, masses and half lives of Sr-90 and daughter nuclei [7].

^{90}Sr primarily emits beta particles during its decay process, making it an important source for various applications, including ionization cameras. The source can also undergo gamma emission due to the two meta-states names as 2^+ and 0^+ corresponding to 2186.3 keV and 1760.7 keV, respectively. The decay spectrum and the absolute decay probabilities have been consulted and taken from the *Nuclear Data Section of the International Atomic Energy Agency* [17].

In MCNP, the source is modelled as a continuous source due to the β^- particles emission. This implies that the energy is distributed in a non-discrete manner between the emitted electron and the residual nucleus. Consequently, different beta decays can

5 Simulated Check Source

produce electrons at different energies within a specific range. The isotropic strontium source is placed in a designated cell, which is in contact with the air and brass, and it emits β^- particles that generates continuous *bremsstrahlung* radiation in all directions.

An accurate geometrical arrangement of the source has been performed conform to the sketch of the *Radioaktive Kontrollvorrichtung 39 Typ 8921 für PTW-Dosimeter* [19] issued by PTW. Both the sketch and the simulated geometry of the source are compared in Figure 5.2

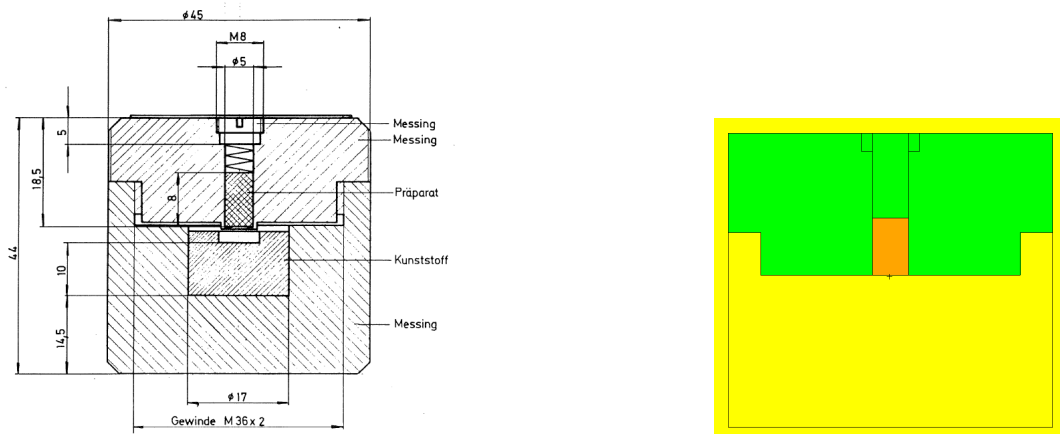


Figure 5.2: Sketch (left) and simulation (right) of the ^{90}Sr source.

The materials are defined conform with the standard established by the compendium of MNCP [20]. In the simulated source plotted in Figure 5.2 (right), the yellow area represents dry air, the green part is composed by brass, and the orange cell is made of Sr-90. In the next table there is exposed a more detailed view of the composition of each material:

Material	Composition	ZAID	Atom fraction
Dry air	C-12	6012.80c	0.000124
	N-14	7014.80c	0.755267
	O-16	8016.80c	0.231781
	Ar-40	18040.80c	0.012827
Brass	Fe	26000.84p	0.000868
	Cu	29000.84p	0.665384
	Zn	30000.84p	0.325699
	Sn	50000.84p	0.002672
	P	82000.84p	0.005377

Table 5.1: MCNP material composition of the dry air and brass [20].

As it is noticeable in the last table, the entire ZAID is included for a more complete reference to the specific atom according to the listing tables of Los Alamos National Laboratory [8]. The density of the dry air at near the sea level altitude is tabulated as 1.205 mg cm^{-3} and for brass, its density is tabulated as 8.07 mg cm^{-3} .

5.2 Activity Calculation

In this subsection, the calculations of the activity of the source are discussed. This step is necessary to set the decay energies and probabilities of the source in the simulated setup.

The production of the ^{90}Sr sample dates from the year 1980 according to *Radioaktive Kontrollvorrichtung 39 Typ 8921 für PTW-Dosimeter* [19]. The exact production date of the radioactive material remains unknown. For the purpose of the calculations, the exact date and initial activity A_0 , that is taken as a reference to obtain the activity of the sample are **0.9 mCi**, this is, 33 MBq.

The only decay mode possible for strontium is β^- decay. The daughter nucleus ^{90}Y , has three potential decay modes into ^{90}Zr , as indicated in the following table sourced from the *International Atomic Energy Agency* [17]:

#	$\langle E\beta^- \rangle$ [keV]	$I\beta^- (\text{abs})$ [%]	Daughter level [keV]	$J\pi$	$E\beta_{\max}^-$ [keV]	Transition type
1	24.2 5	0.0000014	2186.27	2+	92.2	1st non-unique
2	184.6	0.0115	1760.74	0+	517.8	1st unique
3	932.4	99.9885	0	0+	2278.5	1st unique

Table 5.2: Decay paths of $^{90}_{39}\text{Y}$ according to the International Atomic Energy Agency.

The decay listed as 1 has such a very low absolute probability that the yttrium decay path into the most excited state of zirconium has been neglected. It is assumed from this point, that there will be a total of **three** β^- and only **one** γ emission in the entire decay chain. Those are the decays that have been included in the MCNP model of the ^{90}Sr source.

Regarding the β^- decays, these are included in the model only after having the spectra of the strontium and yttrium sampled accordingly to account for the continuous nature of the β^- decay. The γ emission is considered separately in MCNP and only one energy is regarded in our problem as it is a discrete event. Further explanations about the separation and configuration of the energies are given later in this chapter.

From nuclear physics it is known that a parent-daughter nuclear decay chain is ruled by a system of two differential equations describing the particle production rate of the parent and daughter nucleus whose solution [15] for the daughter nucleus is:

$$N_D(t) = \frac{\lambda_P N_P(0)}{\lambda_D - \lambda_P} (e^{-\lambda_P t} - e^{-\lambda_D t}) + N_D(0) e^{-\lambda_D t} \quad (5.1)$$

From Equation 5.1, and taking into account that the half life of the parent is much longer than that of the daughter, it can be concluded that the decay chain reaches a situation known as **secular** equilibrium. This means that both activities reach a

saturation activity after a very long time. This means that the activity of the daughter can be calculated as:

$$A_D(t) = -\frac{dN_D}{dt} = \lambda_D N_D(t) \quad (5.2)$$

In Equation 5.2, the term $\lambda_P N_P(t)$ is not stated because it is neglected as the quantity is much smaller than the term $\lambda_D N_D(t)$ as $\lambda_D > \lambda_P$. Here, the parameters of Equations 5.2 and 5.1 are the same, where λ_P and λ_D stand for the radioactive decay constants calculated from the half lives of the parent (strontium) and daughter (yttrium), respectively. $N_P(0)$ stands for the initial number of nucleus of the strontium. For the strontium sample, i.e. the parent nucleus, the activity is simply calculated according to the radioactive decay law:

$$A_P(t) = \lambda_P N_P(0) e^{-\lambda_P t} \quad (5.3)$$

Taking as the reference date for the calculation of the activities from 5.3 and 5.2 the 5th of July of 2023, it results in 12.02 MBq and 12.018 MBq, respectively. As it is expected from the secular equilibrium, both samples have approximately the same activity.

5.3 Sampling of the Emission Spectrum

The next step to set up the source is to calculate the decay probability of each decay path. For that, it is necessary to know the shape of the beta decay spectra for both samples. According to the atlas of the beta decay spectrum written by the *Institute of Physics and Engineering in Medicine* [9], the spectrum is:

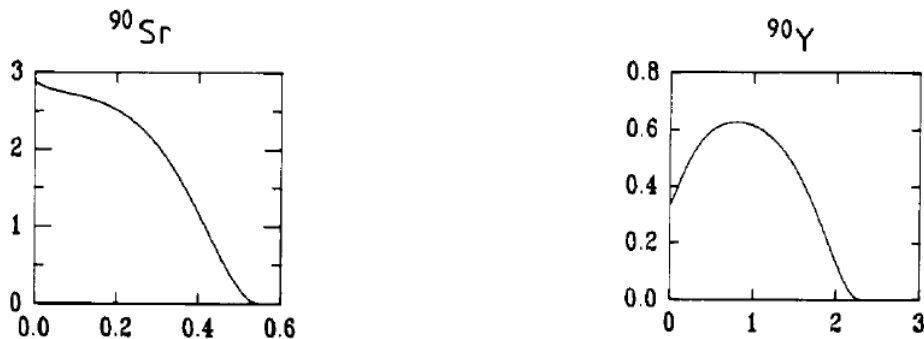


Figure 5.3: Number of beta particles emitted per MeV for one transition of ^{90}Sr (left) and ^{90}Y (right).

Knowing the spectrum of both samples, it is therefore possible to sample the spectrum of emission for both of them and configure the source using multiple

discrete energies together with their probability. To simplify the configuration of the source and avoid stepping into nested probability calculations, the simulation is executed twice: once for each sample whilst assuming 100% decay probability for ^{90}Sr , and once assuming 99.9885 % and 0.0115% decay probability for the processes $^{90}\text{Y} \xrightarrow{\beta^-} {}^{90}\text{Zr}$ and $^{90}\text{Y} \xrightarrow{\beta^-} {}^{90}\text{Zr}^{0+}$, respectively. Only the corresponding probabilities to the energy bins of the β^- processes are taken into account at this point and they are taken from the *International Atomic Energy Agency* [17].

Once each simulation completes, the data for the particle flux and for the dependence of the deposited energy on the density of the corrosion layer is obtained. The data needs an additional **sampling** to account for the activity produced by each (strontium and yttrium) radiation source. As described before, roughly 50% of the total activity comes out of each sample. It is important to note that this last sampling is done after the simulation completes, which means that the only sampling included in MCNP is the sampling of energies that account for each decay path. This sampling make up the values of the next table:

E [MeV]	β^- Sr-90 [%]
0.0137	7.79
0.0410	7.60
0.0683	7.50
0.0956	7.40
0.123	7.30
0.150	7.17
0.177	7.01
0.205	6.80
0.232	6.53
0.259	6.19
0.287	5.78
0.314	5.27
0.341	4.68
0.369	4.01
0.396	3.27
0.423	2.48
0.450	1.71
0.478	0.98
0.505	0.43
0.532	0.10

E [MeV]	β^- Y-90 [%]
0.057	4.26
0.171	5.18
0.286	5.94
0.400	6.50
0.514	6.87
0.628	7.08
0.742	7.17
0.857	7.15
0.971	7.04
1.080	6.85
1.200	6.57
1.310	6.19
1.430	5.69
1.540	5.07
1.660	4.30
1.770	3.42
1.880	2.46
2.000	1.50
2.110	0.64
2.230	0.11

Table 5.3: Decay probabilities of strontium (left) and yttrium (right). In the Y-90 table, the decay to the ground excited state has not been included along with its probability.

The values listed on Table 5.3 complete the definition of the source in MCNP after the probabilities are normalized to the unit. The decay path of the excited state is not included in the table although it is set in the definition of the source along with the values of Table 5.3. Attending to the description of the decays of the *International Atomic Energy Agency* [17], the process ${}^{90}\text{Y} \xrightarrow{\beta^-} {}^{90}\text{Zr}^{0+}$ takes place at 184.6 keV with a probability of 0.0115 %.

The next decay, ${}^{90}\text{Zr}^{0+} \xrightarrow{\gamma} {}^{90}\text{Zr}$, is the only gamma decay that is considered in the analysis of the decay chain and happens at an energy of 1.76 MeV [17]. Its probability, in turn, is taken as 100 % i.e. the same probability as for the process ${}^{90}\text{Y} \xrightarrow{\beta^-} {}^{90}\text{Zr}^{0+}$ i.e. 0.0115% since we are neglecting the most upper exited state pictured in Figure 5.1. For this particular γ transition, a separate line spectrum has been set up in MCNP to generate only photons. However, it is included in the bins of the input of MCNP to cover the excited state. The probabilities for Sr – 90 and Y – 90 that are listed on Table 5.3 are normalized to the unit and those are the values used in the MCNP source configuration.

5.4 Setting up the soure

After having modelled the source and its materials, the MCNP simulation runs the described source placed 2.65 cm away from the outermost part of the ionization chamber in its transversal direction and pointing to the chamber. Finally, the geometry of the source was replicated using translation cards of MCNP in its mirror position to match the experimental configuration. The view in the XY plane of the arrangement set to run at the desired number of particles is:

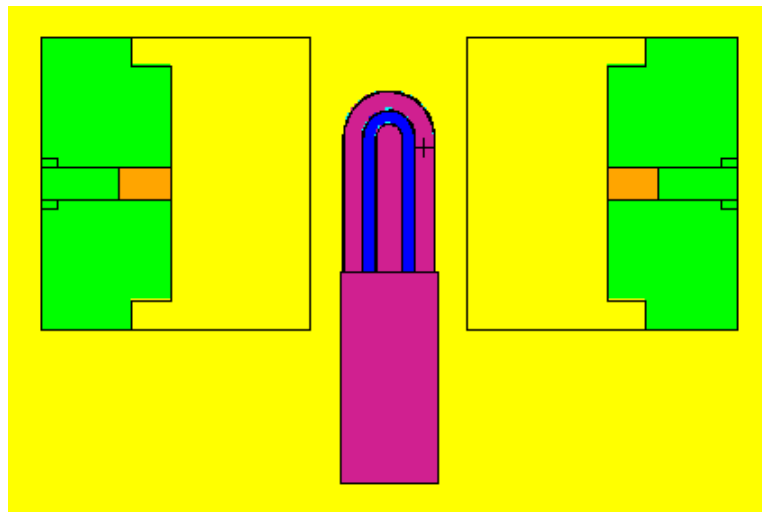


Figure 5.4: Geometrical arrangement of the simulated ${}^{90}\text{Sr}$ source and the PTW TM33054 magnesium chamber.

The closest line of the source to the chamber is not a wall and must not be understood as an edge with which the particles interact once they are emitted. Planes are meant to define the cells and are not made of any material themselves. The line is just an MCNP plane that needs to be set up to define the cell and fill it with air.

Both sources and the chamber are placed in a wooden structure that holds all three devices in the presented position and given the dimensions of the setup, the presence of the frame will not produce a measurable significant effect in the dose deposited in the argon gas inside the chamber.

For security reasons and due to the regulations of *FRM II* regarding the access to the facilities, it is unfortunately not possible to include in the present work a photo of the actual set of frame, sources and chamber to evidence its differences with our simulation.

To visualize the particle flux in the MCNP geometry, the simulation needs to be run using the *FMESH* card. It sets a grid around the entire setup. The result of the test is:

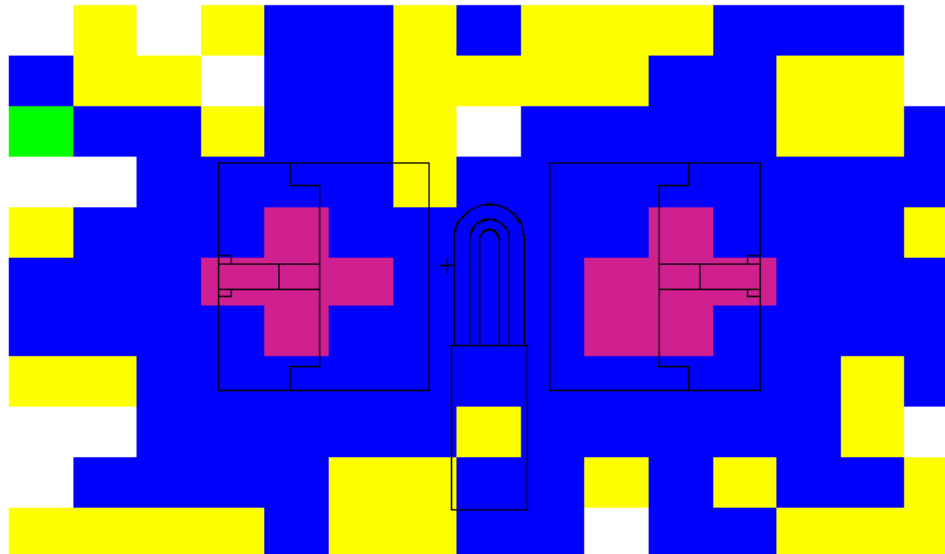


Figure 5.5: Particle flux in empty geometry.

The interpretation of Figure 5.5 relies on understanding the color scheme employed by MCNP. The color purple is assigned to the region with the highest particle concentration, while blue, yellow, and green represent progressively lower incidences of particles. In Figure 5.5 it is evidenced that any intensity of the flux of particles that stems from the cells where the source is set up lies around that cell and propagates towards the position of the chamber. Hence, all cells are geometrically correct and the simulation is ready to run.

5.5 Bremsstrahlung spectrum

The goal of this section is to study the *bremsstrahlung* spectrum of the source in order to take its photons into account for the configuration of the check source. In the source, mainly electrons come out of the source cells and only the γ photon. When electrons exit the cell containing Sr-90 and come into contact with the ionization chamber filled with argon, a phenomenon known as *bremsstrahlung* occurs. *Bremsstrahlung*, which means "braking radiation" in German, refers to the electromagnetic radiation emitted by charged particles when they experience acceleration or deceleration. This radiation can also arise from the interaction of the electrons with the dry air.

In this particular scenario, as the electrons from Sr-90 move through the ionization chamber interact with the atoms of air on their way to the chamber and then, with the sequence of layers of materials until they reach the argon present within the chamber. These interactions cause the electrons to undergo acceleration or deceleration due to the electromagnetic forces between the charged particles.

During the acceleration or deceleration process, the electrons emit *bremsstrahlung* radiation. This radiation encompasses a wide range of energies, spanning from low-frequency radio waves to high-energy X-rays or gamma rays, depending on the magnitude of the electron acceleration.

5.5.1 Particle Flux

To study the generation of secondary photons i.e. *bremsstrahlung* radiation, the simulation is first executed removing all materials and setting them to dry air with the corresponding density of 1.205 mg cm^{-3} . Then, the particle flux is tallied in the same region where the sensitive region of the ionization chamber is placed. The result obtained is a direct measure of the intensity of the radiation source.

This first execution is intended to provide an insight into the natural breaking radiation caused by the interaction of the electrons with the air. According to Section 5.3, the emission spectrum is to be normalized to the activity of the samples. Additionally, the flux is normalized to the first particle to ease the understanding of the plot.

Before simulating the particle production to study its interaction in dry air, it needs to be checked that the particle flux matches the theoretical spectrum, i.e. the spectrum entered as input in the configuration of the source. For this purpose, the simulation is executed once using the *VOID* card in MCNP as before to check the *FMESH* tally. The expected result is pictured in the next plot, as there are no interactions to account for.

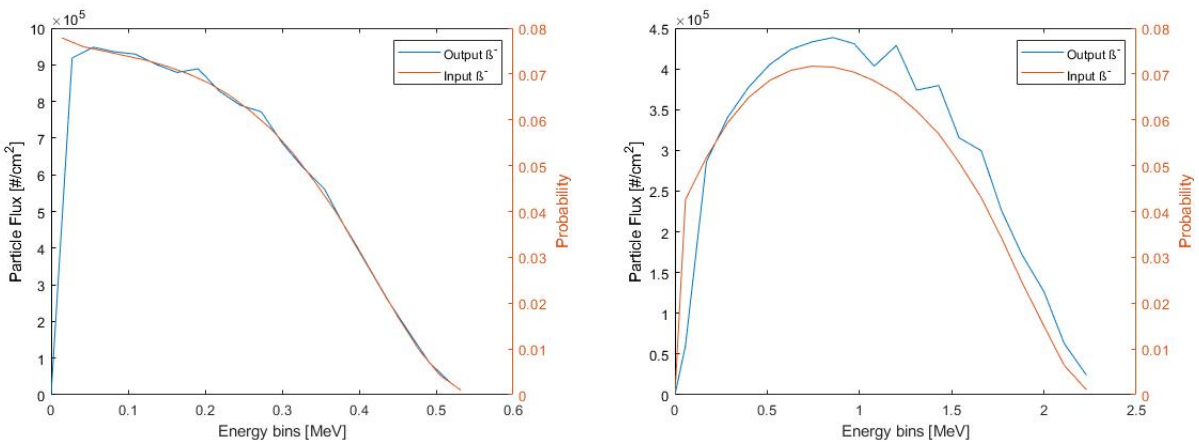


Figure 5.6: Particle flux in vacuum of ^{90}Sr (left) and ^{90}Y (right).

Theoretically, the output should be identical to the input spectrum. Even though there are no interactions to consider, the MCNP statistics might produce a small misalignment between the lines of both plots. It is important to mention that the simulated spectrum is obtained using histogram statistics in MCNP and it has required the data to be centered in the right energy bin. This correction is implemented beforehand by applying the relation $E_i = E_i + \frac{\Delta E}{2}$, where E_i is each energy bin and ΔE is the difference between each bin and the up next. In the yttrium plot, a further correction is applied to improve the smoothness of the output. The result shows a fluctuation around 1 and 1.6 MeV that comes from the statistics applied automatically by the simulation. This effect must be caused by the MCNP statistics and removing it by applying certain correction factors for visualisation purposes does not provide any further valuable insights into the understanding of the behaviour in vacuum.

In Figure 5.6, it is evident that the strontium spectrum lacks any photon emissions, which is expected since strontium decay does not produce photons. Due to the void geometry, there are no interactions between electrons and other particles, thereby ruling out the possibility of any secondary photon production under these conditions.

In contrast, the yttrium decay leads to a **single gamma** photon emission at 1.76 MeV, as specified in the source configuration. This photon is not shown on the graph because the probability is so low that the particle flux is barely noticeable when plotted along with the electron output.

A different behaviour becomes evident if all cells except those adjacent to the source are filled with air. In such case, there is production of secondary photons and, therefore, the electrons emitted by the source also decrease their intensity as many of them undergo the deflection that causes the *bremsstrahlung*.

The simulation result after running at 10^8 particles is:

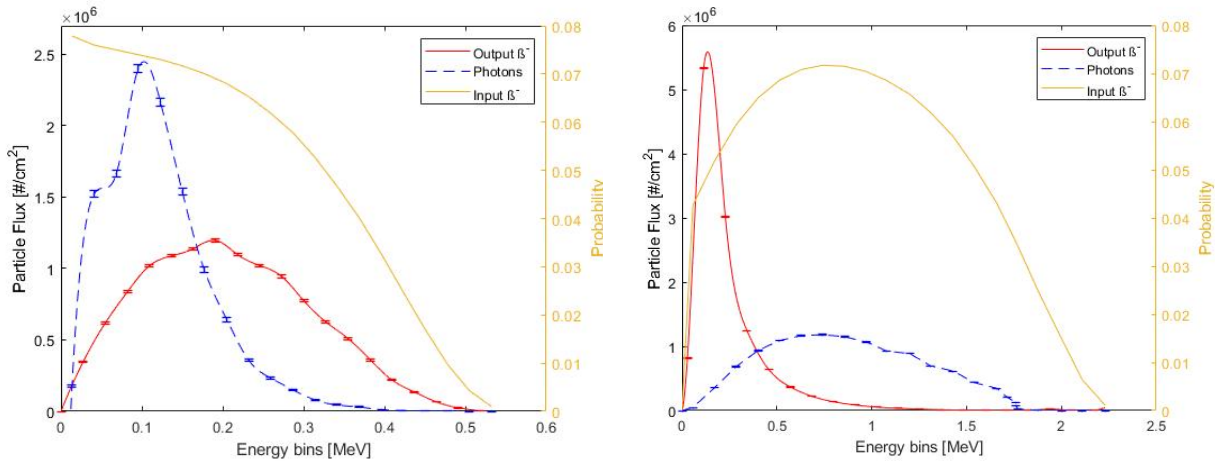


Figure 5.7: Particle flux in air of ^{90}Sr (left plot) and ^{90}Y (right plot) against the energy bin. The right axis is the β^- decay probability of strontium and yttrium in each energy bin, referred to as "Input β^- ". These values serve as input for the *SDEF* card of MCNP. The left axis is the particle flux i.e. intensity of the radiation measured in number of particles that move through each cm^2 of surface.

In Figure 5.7, the particle flux has been normalized to the activity of the sample on the specified date, as mentioned after Equation 5.3. To supplement representation of data, the electron output and photon flux have been interpolated using the *spline* method. However, only the points that have an error bar are the actual data that the simulation returned. Here, the only data that has not been interpolated for practical reasons due to its values is the photon flux for yttrium, shown on the right graph.

Figure 5.7 presents the photon outcomes for both samples. Unlike the vacuum scenario shown in Figure 5.6, it is observed that the flux is no longer negligible for the case of strontium. This change is attributed to the interaction of electrons with the dry air, as previously mentioned. Notably, the *bremsstrahlung* production becomes more pronounced around 100 keV and decreases rapidly after 150 keV.

For yttrium, there is also *bremsstrahlung* production in the low-energy region around 280 keV. The energy that peaks above 0.35 particles per square centimeter corresponds to 1.76 MeV and aligns with the discrete energy input bin specified in the input of MCNP.

In conclusion, the analysis of the *bremsstrahlung* spectrum reveals the formation of secondary photons at various energy levels. The spectrum of the incident electron with energies of 100 keV, 150 keV, and 280 keV exhibit distinctive secondary photon peaks, each reflecting specific energy interactions between the incident electrons and the surrounding air. The secondary photons formed are predominantly X-rays with

the exception of the *gamma* photons of the order of MeV that is produced directly in the yttrium sample and is, therefore, not part of the *bremstrahlung* spectrum.

Lastly, for comparison purposes, the spectrum of both samples according to the live chart of Nuclides from the *International Atomic Energy Agency* is presented in the next figure. According to *Laboratory, L.A.N.: International Atomic Energy Agency* [17], the spectrum is:

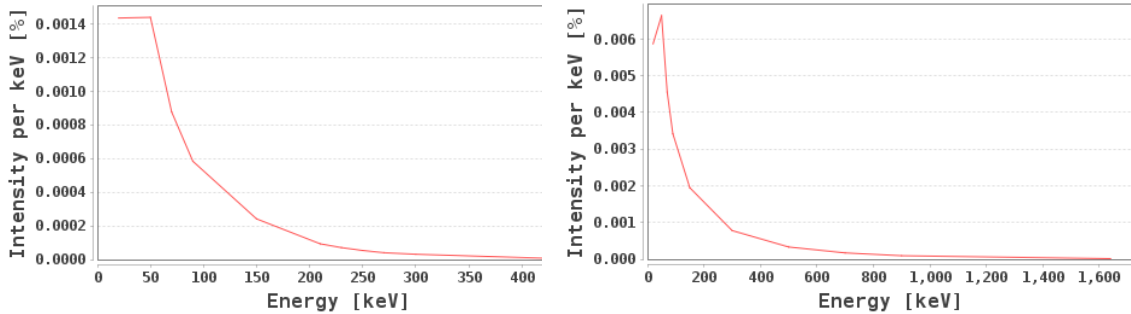


Figure 5.8: Bremsstrahlung spectrum of ^{90}Sr (left) and ^{90}Y (right)

In the right plot, the spectrum is divided into energy bins ranging from 0 to 2.3 MeV, with corresponding intensities. Notably, the breaking radiation of yttrium has a higher intensity in the lower energy ranges (40-100 keV), demonstrating a decreasing trend as energy increases. This matches the expected behavior of *bremstrahlung* radiation and the result presented in this subsection. The photon particle flux is higher in the lower energy region and almost negligible for the higher energies. The same conclusion is reached for the strontium. In this case, the maximum intensity agrees with the simulated spectrum shown in Figure 5.7.

Finally, the check source is configured in MCNP according the probabilities calculated earlier in this chapter, the geometry and relative positions of the source and the chamber, and the breaking radiation spectrum discussed in this last section.

5.6 Simulation

In the last section of this chapter the result of the simulation of the Sr-90 source as described up to this point is presented. The purpose is to study the dose deposition in the PTW chamber TM33053 when it is irradiated by a β^- source. In this simulation, the chamber has the same corrosion layer as the simulations presented in Chapter 3.

The tally +F6 is:

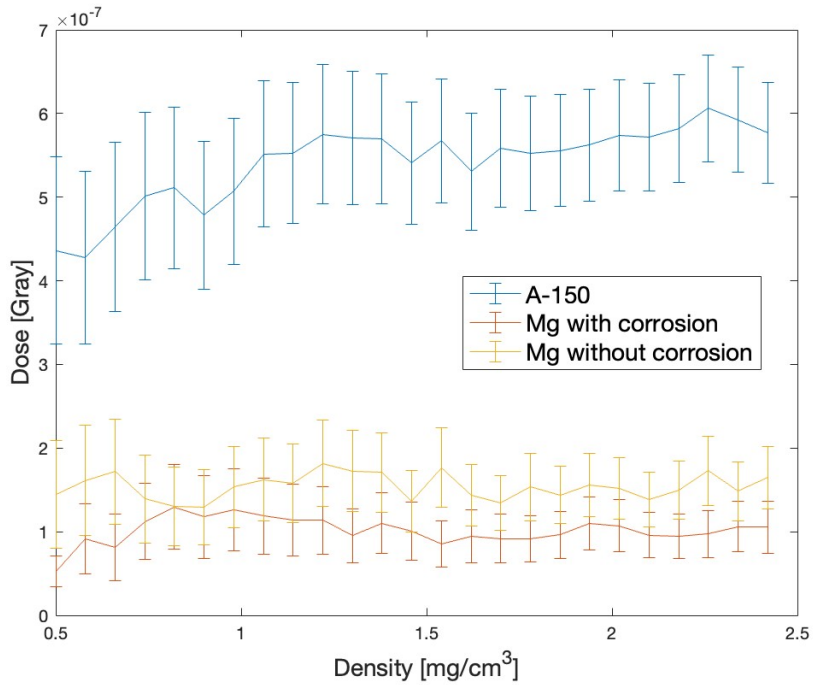


Figure 5.9: Simulation of PTW-33053 with a 0.37 mm thick layer of hydromagnesite on all magnesium surfaces using the check source, without a corrosion layer, and TE chamber. The magnesium chamber has been simulated without a concentration of water. Tally +F6.

It is shown in Figure 5.9 that the dose deposition in the magnesium chamber is constant along the density of argon and almost the same for the simulation with and without the corrosion layer. This is the expected response.

The result of the TM33053 chamber is also expected. The dose in the TE chamber is although of the same order of magnitude, higher than the magnesium chamber. This outcome is due to the higher sensibility of this chamber, as it has been confirmed in the PTB calibration. On the other hand, it is due to the higher complexity of the composition of the A-150 tissue equivalent plastic in comparison with magnesium.

In conclusion, the β^- source can continue to be used as a check source for daily measurements on a magnesium chamber, disregarding the presence of a corrosion layer.

6 Conclusions and Outlook

The results described in this work show that there is a corrosion layer that has built up over the magnesium surface of the PTW TM33054 ionization chamber. This corrosion layer has developed up to a thickness of 0.37 mm. The composition of this layer is not assessable using the neutron CT scan that has been used to estimate the thickness. For this reason, the layer has been assumed to be made of hydromagnesite, which is a mineral that builds up on magnesium under normal atmospheric conditions. It has been found in the MCNP simulations, that the dose absorbed by the sensitive region of the chamber is about 1.5 times higher when a hydromagnesite corrosion layer is present over the magnesium, providing that the regular MEDAPP source is used. The corrosion layer facilitates the energy absorption under the neutron field of the MEDAPP source. Furthermore, it has been found that the total energy deposited in the gas region always increases linearly with the density of the gas, remaining almost constant when only the neutron source is applied. The presence of water in the corrosion layer plays an important role in the dose. Higher concentration of water leads to a higher dose absorption from both radiation sources. For a water concentration of 0 to 3 %, the doses differ in 10 % in the case of a neutron source, and 5 % in case of the regular MEDAPP source.

The corrosion layer is the cause of the increase of the sensibility of the ionization chamber PTW TM33054, which leads to an increased dose. This chamber is assumed to increase its k_U value over the years, and it has been confirmed in the calibration performed in this thesis that the sensibility of the PTW TM33054 chamber has risen from 0.155 to 0.202 since 2018 to 2023. This increase has attributed a shift in the measured dose.

The chambers TE-13 and TE-14 are assumed to have a constant sensibility. The outcome of the calibration challenges that assumption as the value of k_T has been measured to be 1.031 and 1.038, respectively. There is a build-up effect to account for in the tissue equivalent plastic chambers. However, the effect is negligible for all energies below 2.5 MeV.

The change in the neutron sensibility is not visible in the check source measurements.

Future work could focus on an in-depth analysis of the corrosion layer composition through additional chemical studies, offering a more in-depth understanding of the materials involved under varied atmospheric conditions. Long-term sensibility studies are necessary to monitor the evolution of ionization chamber sensibility over extended periods, emphasizing periodic calibration of the chambers to account for the development of the corrosion layer. Additionally, exploring the influence of corrosion layers on the sensibility of the chambers under different energy ranges, especially in

6 Conclusions and Outlook

scenarios with neutron energies within the range of application for therapy treatments, would contribute to a more comprehensive understanding of the system's response.

Acknowledgments

Throughout this work many people have contributed in some extent to successfully conclude the discussions. This project has been possible thanks to the expertise of Dr. Lucas Sommer, Dr. Tobias Chemnitz at FRM II and Prof. Dr. Peter Müller-Buschbaum. I would like to thank Dr. Lucas Sommer for the extensive discussions on the neutron dosimetry simulations and Dr. Tobias Chemnitz for the continuous supervision of the results of this work.

The multiple simulations have been performed using the Monte Carlo N-Particle code, which has been developed, maintained and delivered by Los Alamos National Laboratory. MCNP models of the radiation source used at MEDAPP were provided by Dr. rer. nat. Harald Breitkrutz, which completed the simulation of the MEDAPP facilities. Without the simulation software, this dissertation would have not been possible. Special thanks to the LANL development team for making the software possible.

The multiple simulations have been automated using an automation tool developed in Python in IntelliJ. This application has significantly facilitated the analysis of data returned by MCNP and made a fundamental contribution to this project. Without this application and the processing infrastructure, it would have not been possible to obtain the results presented in this work within the time span required by the Technical University of Munich.

The calibration measurements of the ionization chambers have been performed at Physikalisch-Technische Bundesanstalt in Braunschweig. The measurements were possible thanks to the collaboration of Dr. Ralf Nolte, Dr. Lucas Sommer and Dr. Tobias Chemnitz over the course of a week to accurately install the devices and set-up the radiation source.

Again, I would like to thank Dr. Tobias Chemnitz for giving me the opportunity to participate in this project and Prof. Dr. Peter Müller-Buschbaum for accepting supervising this thesis.

List of Figures

2.1	Basic design of a Farmer Ionization Chamber.	6
3.1	X-ray CT scan of EXRADIN chamber (left) and the PTW TM33054 chamber (right). Both devices are made of magnesium.	14
3.2	Image of the X-ray CT scan of the PTW TM33054 ionization chamber. .	15
3.3	Neutron scan of TM33054 (left) and CT values vs. distance plot (right). .	15
3.4	Simulated PTW chamber (left) and a close-up of the tip of the chamber (right). In the close-up, it is noticeable that a layer of hydromagnesite, shown in green, is added to the surface of the anode and to the inner part of the wall. The scale bar has been placed at the bottom of both images.	16
3.5	Simulation of PTW TM33054 with a 0.37 mm thick layer of hydromagnesite on all magnesium surfaces. Tally +F6. In the legend the fraction of water is stated in percentages.	18
3.6	Energy deposition in the sensitive region of the PTW TM33054 chamber with a hydromagnesite layer.	19
3.7	Dose delivered by neutrons in the sensitive region of the PTW TM33054 chamber with a 0.37 mm thick hydromagnesite layer.	20
3.8	Simulation of PTW TM33054 with a 0.37 mm thick layer of hydromagnesite on all magnesium surfaces. Electron and proton contribution.	21
3.9	Simulation of PTW TM33054 with a 0.37 mm thick layer of hydromagnesite on all magnesium surfaces using the MEDAPP neutron source. Tally +F6. In the legend the fraction of water is stated in percentages.	22
3.10	Energy deposition in the sensitive region of the PTW TM33054 chamber with a hydromagnesite layer using the MEDAPP neutron source.	23
3.11	Simulation of PTW TM33054 with a 0.37 mm thick layer of hydromagnesite on all magnesium surfaces using the MEDAPP neutron source. Neutron contribution.	24
3.12	Simulation of PTW TM33054 with a 0.37 mm thick layer of hydromagnesite on all magnesium surfaces. Electron and proton contribution.	25
4.1	Picture of a ionization chamber set up at PTB Braunschweig. The chamber is located in the middle and set up vertically. On the right side, the radiation source is pointing perpendicularly to the tip of the chamber.	28
4.2	Values of k_U and k_T measured at PTB in different years for 2.5 MeV. . .	30

4.3	Cross section measured in <i>barns</i> of various selected isotopes as a function of neutron energy.	31
4.4	Energy deposition plot of a TE cylinder plot using a plane neutron source at different energies. There is no gap between the source plane and the cylinder.	32
4.5	Energy deposition plot of the magnesium cylinder plot using a plane neutron source at different energies. There is no gap between the source plane and the cylinder.	33
4.6	Close-up of the energy deposition plot of the magnesium cylinder plot using a plane neutron source at different energies. There is no gap between the source plane and the cylinder.	34
4.7	MCNP plot of the cross section in <i>barns</i> of Mg.	35
5.1	Decay scheme of Sr-90, masses and half lives of Sr-90 and daughter nuclei [7].	37
5.2	Sketch (left) and simulation (right) of the ^{90}Sr source.	38
5.3	Number of beta particles emitted per MeV for one transition of ^{90}Sr (left) and ^{90}Y (right).	40
5.4	Geometrical arrangement of the simulated ^{90}Sr source and the PTW TM33054 magnesium chamber.	42
5.5	Particle flux in empty geometry.	43
5.6	Particle flux in vacuum of ^{90}Sr (left) and ^{90}Y (right).	45
5.7	Particle flux in air of ^{90}Sr (left plot) and ^{90}Y (right plot) against the energy bin. The right axis is the β^- decay probability of strontium and yttrium in each energy bin, referred to as "Input β^- ". These values serve as input for the SDEF card of MCNP. The left axis is the particle flux i.e. intensity of the radiation measured in number of particles that move through each cm^2 of surface.	46
5.8	Bremsstrahlung spectrum of ^{90}Sr (left) and ^{90}Y (right)	47
5.9	Simulation of PTW-33053 with a 0.37 mm thick layer of hydromagnesite on all magnesium surfaces using the check source, without a corrosion layer, and TE chamber. The magnesium chamber has been simulated without a concentration of water. Tally +F6.	48

List of Tables

3.1	Density of the hydromagnesite composite accounting for a percentage of water.	17
3.2	Slope comparison of the linear fit for the energy deposition of the MEDAPP source in PTW TM33054. No corrosion corresponds to the simulation of the chamber where no corrosion layer has been included.	19
3.3	Slope comparison of the linear fit for the energy deposition of the MEDAPP neutron source in PTW TM33054. No corrosion corresponds to the simulation of the chamber where no corrosion layer is included.	23
4.1	Constants used in Equation 4.1.	28
4.2	Calculated k_T and k_U for the PTW tissue equivalent and magnesium chambers at 1.2 MeV, respectively.	29
4.3	Calculated k_T and k_U for the PTW tissue equivalent and magnesium chambers at 2.5 MeV, respectively.	29
4.4	Slope comparison of the linear fit for the sensibility of the chambers TE-13, TE-14 and Mg-01 at 2.5 MeV.	31
5.1	MCNP material composition of the dry air and brass [20].	38
5.2	Decay paths of $^{90}_{39}\text{Y}$ according to the International Atomic Energy Agency.	39
5.3	Decay probabilities of strontium (left) and yttrium (right). In the Y-90 table, the decay to the ground excited state has not been included along with its probability.	41

Bibliography

- [1] Nist star (stopping power and range tables for electrons, protons, and helium ions). <http://physics.nist.gov/Star>. Accessed: January 2023
- [2] Webmineral. <http://www.webmineral.com/> (1996). Accessed: April 2023
- [3] PtW dosimetry - farmer ionization chambers 30010. <https://www.ptwdosimetry.com/en/products/farmer-ionization-chambers-30010> (2023). Accessed: July 2023
- [4] AAPM: Protocol for Neutron Beam Dosimetry (1980)
- [5] Adrian Barbu, S.C.Z.: Monte Carlo Methods (2020)
- [6] Aird, E.G.A., Farmer, F.T.: The design of a thimble chamber for the farmer dosemeter. Physics in Medicine Biology **17**(2), 169 (1972). DOI 10.1088/0031-9155/17/2/001. URL <https://dx.doi.org/10.1088/0031-9155/17/2/001>
- [7] Boeglin, W.: Modern Lab Experiments. Chapter 4: Beta Spectroscopy (2023)
- [8] Conlin, J.L., Parsons, D.K., Gardiner, S.J., Gray, M.G., Kahler III, A.C., White, M.C., Lee, M.B.: Listing of available ace data tables. Tech. rep., Los Alamos National Lab.(LANL), Los Alamos, NM (United States) (2014)
- [9] Cross, W.G.: A short atlas of beta ray spectra (1983)
- [10] Dinesh K. Aswal Partha S. Sarkar, Y.S.K.: Neutron Imaging. (2022)
- [11] Ferbel, D.: Introduction to Nuclear and Particle Physics (2003)
- [12] Forschungszentrum Jülich: MlZ garching - radiotherapy and biology (2022). URL <https://mlz-garching.de/englisch/industry-und-medicine/radiotherapy-und-biology.html>. Accessed: February 2023
- [13] Gray, L.H.: An Ionization Method for the Absolute Measurement of γ -Ray Energy. Proceedings of the Royal Society of London. Series A-Mathematical and Physical Sciences **156**(889), 578–596 (1936)
- [14] Jönsson, M.: The atmospheric corrosion of magnesium alloys: Influence of microstructure and environments. Ph.D. thesis, KTH (2007)

Bibliography

- [15] Juan, P.M.: Lecture notes of applications of radioactivity in industry, research and medicine (2022)
- [16] Kühn, D.: Ionization chambers for neutron dosimetry.
- [17] Laboratory, L.A.N.: International Atomic Energy Agency - Nuclear Data Section - <https://www-nds.iaea.org/> (2007-2023)
- [18] Podgorsak, E.B.: Radiation oncology physics (2005)
- [19] PTW Freiburg, P.T.W.D.P.G.: Radioaktive Kontrollvorrichtung 39 Typ 8921 für PTW-Dosimeter (1994)
- [20] R.G. Williams III C.J. Gesh, R.P.: Compendium of Material Composition Data for Radiation Transport Modeling (2006)
- [21] Rinard, P.: Neutron Interactions with Matter. Passive Nondestructive Assay of Nuclear Materials (375-377) (1991)
- [22] Sommer, L.B.: Bestimmung des Neutronen-Ansprechverhaltens einer Mg- und einer Al-Mg-Ionisationskammer relativ zu einer TE-Kammer in einem quasi-monoenergetischen Neutronenstrahl der PTB in Braunschweig (2018)
- [23] Sommer, L.B.: Development and validation of a 3d neutron therapy treatment planning software for frm ii. Ph.D. thesis, Technische Universität München (2022)
- [24] Turner, J.E.: Atoms, Radiation and Radiation Protection. (2014)
- [25] Wagner, F., Kampfer, S., Kneschaurek, P.: Bericht zur Basisdosimetrie für medizinische Bestrahlung an der Strahlkonverteranlage am FRM II in Garching. (2006)
- [26] Wagner, F.M., Breitkreutz, H., Loeper-Kabasakal, B., Specht, H.: Fast Neutron Therapy: A Status Report. Sibirskiy Onkologicheskiy Zhurnal **6**(IMPULSE-2017-00167), 5–12 (2015)
- [27] Wagner, F.M., Kneschaurek, P., Kastenmüller, A., Loeper-Kabasakal, B., Kampfer, S., Breitkreutz, H., Waschkowski, W., Molls, M., Petry, W.: The Munich Fission Neutron Therapy Facility MEDAPP at the Research Reactor FRM II. Strahlentherapie und Onkologie **184**(12), 643–646 (2008)
- [28] X-5 Monte Carlo Team: MCNP A General Monte Carlo N-Particle Transport Code Version 5 Volume I: Overview and Theory. Los Alamos National Laboratory, Los Alamos, NM, LA-UR-03-1987 (2003)
- [29] X-5 Monte Carlo Team: MCNP A General Monte Carlo N-Particle Transport Code Version 6.2. Los Alamos National Laboratory, Los Alamos, NM, LA-UR-03-1987 (2003)